Copper Doping of Zinc Oxide by Nuclear Transmutation

THESIS

Matthew C. Recker, Captain, USAF

AFIT-ENP-14-M-30

DEPARTMENT OF THE AIR FORCE
AIR UNIVERSITY

AIR FORCE INSTITUTE OF TECHNOLOGY

Wright-Patterson Air Force Base, Ohio

AFIT-ENP-14-M-30

COPPER DOPING OF ZINC OXIDE BY NUCLEAR TRANSMUTATION

THESIS

Presented to the Faculty

Department of Engineering Physics

Graduate School of Engineering and Management

Air Force Institute of Technology

Air University

Air Education and Training Command

in Partial Fulfillment of the Requirements for the

Degree of Master of Science

Matthew C. Recker, BS

Captain, USAF

March 27th, 2014

AFIT-ENP-14-M-30

COPPER DOPING OF ZINC OXIDE BY NUCLEAR TRANSMUTATION

Matthew C. Recker, BS
Captain, USAF

Approved:

//signed//	27 February 2014
John W. McClory, PhD (Chairman)	Date
//signed//	27 February 2014
James C. Petrosky, PhD (Member)	Date
//signed//	27 February 2014
Robert L. Hengehold, PhD (Member)	Date

Abstract

This research verifies that neutron irradiation of zinc oxide leads to Cu-doping of the material by nuclear transmutation. When irradiated, the zinc atoms in ZnO can absorb a neutron resulting in four unstable isotopes (^{65}Zn, ^{69}Zn, ^{69m}Zn and ^{71}Zn) which will decay according to their half-lives. ^{71}Zn has a very short half-life and ^{69}Zn decays via a non-gamma emitting β-emission, so neither of these isotopes were detected with gamma spectroscopy. However, both ^{65}Zn and ^{69m}Zn were detected and positively identified. ^{65}Zn was visible at all times and ^{69m}Zn was visible when the samples were measured within a few days of irradiation. All decay paths of ^{65}Zn lead to ^{65}Cu and the detection of the 1115.5 keV characteristic γ-ray from this decay clearly indicated that ^{65}Cu was being created.

Previous electron paramagnetic resonance (EPR) spectroscopic results were replicated to determine the spectrum of copper impurities in ZnO as well as the corresponding spacing between signals for the two stable isotopes of copper. This hyperfine spacing was found to be 1015±1 G for ^{65}Cu and 947±1 G for ^{63}Cu. The separation between the signals for the irradiated samples was found to be 1013±1 G confirming the creation of only ^{65}Cu, as predicted by theory.

One motivator for this research was to produce p-type ZnO material through the introduction of copper atoms. The copper EPR signal detected in this research was visible without light stimulation at 6 K, indicating the copper atoms created by transmutation are in the Cu^{2+} state. This implies that these copper atoms exist above the Fermi level. However, there is not enough evidence to determine the position within the band gap and its suitability for p-type material remains undetermined.

This thesis is dedicated to my family.

Thank you for your love, support and understanding throughout my research!

Acknowledgements

I would like to thank Dr. John McClory for serving as the chair of my Thesis Committee as well as providing support through valuable insight and guidance. I'd like to thank my committee members: Dr. Petrosky and Dr. Hengehold. I thank Dr. Halliburton for suggesting this research topic and his full support in all of the EPR aspects. I thank Capt Shamaun Holston for all of his help in the EPR lab. Finally, I thank Kevin Herminghuysen and everyone at the Ohio State University Research Reactor for their time and expertise.

Matthew C. Recker

Table of Contents

Page

List of Figures

Figure Page

List of Tables

COPPER DOPING OF ZINC OXIDE BY NUCLEAR TRANSMUTATION

I. Introduction

1.1 Motivation

Zinc oxide has traditionally been used in its polycrystalline form and is a component of many electronic devices including varistors, transducers, phosphors and transparent films. However, the growth of single crystal ZnO has been improving since the 1990s and interest in studying its single crystalline form has likewise increased [1]. Its wide band gap (3.4 eV) and ability to emit UV light are of great interest, but p-type ZnO is needed to improve efficiency for UV lasing [2]. Doping ZnO with Cu has been proposed as a method for creating p-type ZnO [2] and this research examines Cu-doping of zinc oxide by nuclear transmutation, a process referred to as nuclear transmutation doping (NTD) in which a ^{64}Zn nucleus absorbs a neutron and ultimately transmutes to ^{65}Cu.

NTD is a potentially desirable method for introducing the copper due to the controllability of the doping concentration and the uniformity and positioning of the dopant. Insufficient dopant in the material is easily fixed by re-irradiating the sample with additional neutrons until the proper doping level is reached. Historically, NTD has been applied to doping silicon with phosphorus at a large industrial scale in both the United States and the former Soviet Union resulting in the production of hundreds of tons of material annually [3, 4].

1.2 Previous Studies

Two groups have recently investigate doping ZnO with copper by nuclear transmutation, but their results were inconclusive [2, 5]. A difficulty in proving the presence of copper is the long half-life for the decay of ^{65}Zn (244 days). The samples must be allowed to decay for a long time in order to measure the copper directly using photoluminescence (PL) or infrared (IR) absorption, and even then the concentration of newly formed copper in the samples will be low, relative to the quantity of copper impurity normally present in the growth of ZnO, and thus difficult to detect.

1.2.1 Korea University (2003)

In 2003, researchers at Korea University irradiated 3 samples for 0.5 hours, 24 hours and 168 hours with a high thermal neutron flux, $3.4 \times 10^{16} \frac{neutrons}{cm^2\, s}$, and a correspondingly low fast neutron flux [5]. These samples were then examined with PL in an attempt to show ^{65}Cu had been produced. Their spectra have a small fluctuation due to the presence of copper, but the spectra from their irradiated samples are nearly identical to their unirradiated sample [5].

1.2.2 Washington State University (2011)

In 2011, researchers at Washington State University looked at the same problem and used IR absorbance to show that copper had been created in their samples of ZnO. They irradiated two samples for 4.5 hours and 45 hours with a flux of $4 \times 10^{12} \frac{thermal\, neutrons}{cm^2\, s}$. Their first sample showed no copper, while the other showed an IR signal that was slightly above background with a signal-to-noise ratio of about $\frac{2}{1}$ [2]. Of concern is the amount of time between irradiation and the measurement of IR absorbance, which was not mentioned in their journal article. This timing is important because the long half-life of ^{65}Zn may require a long period after irradiation

for a detectable concentration of copper to seen using this method.

1.3 Zinc Oxide Applications

ZnO has many properties that could lead to important applications. With its wide band gap and large exciton energy, ZnO has been a prime candidate material for UV lasing and blue light-emitting diodes, but p-type ZnO is needed to fully realize these [1, 6]. Cu-doping of ZnO has been proposed as a method of producing p-type material [2], but the EPR results in this research suggest that Cu is a deep acceptor and will not be able to increase the p-like nature of the material.

Another possible use for Cu-doped ZnO is in spintronics as a diluted magnetic semiconductor (DMS). Several publications have suggested that copper doped into ZnO will create ferromagnetic behavior that might be used to create a DMS [7–9]. However, some articles have been unable to find any ferromagnetic behavior in Cu-doped ZnO [10]. Copper is interesting as a dopant because its Cu^{2+} state has an unpaired electron which leads to a magnetic moment, but Cu, CuO and Cu_2O have no ferromagnetic properties. This means that any ferromagnetic behavior seen will be due to the substitution of Cu on Zn sites and not a result of clustering [7–9]. Furthermore, the wide band gap of ZnO means that these semiconductors could be operated at or near room temperature. If these positive results are confirmed, then Cu-doped ZnO may become important as a DMS material in a spin-based transistor and NTD would be a great mechanism for introduction of the dopant.

1.4 Thesis Objectives

Previous attempts to study the Cu-doping of ZnO by NTD have insufficiently demonstrated that copper has been created in the crystals. These efforts have focused on IR absorbance [2] or photoluminescence (PL) [5] measurements and resulted in

signals that were not much above background levels. However, the science behind transmutation is sound.

The first objective of this research is to irradiate samples of single-crystal ZnO and detect the transmutation of ^{64}Zn nuclei into ^{65}Cu nuclei. High purity samples of zinc oxide grown by Eagle Picher, using the chemical vapor transport (CVT) technique, as well as samples from Airtron and Tokyo Denpa produced using a hydrothermal growth method, will be irradiated at the Ohio State University Research Reactor (OSURR) for several hours. According to theory, ^{64}Zn atoms will absorb neutrons to form ^{65}Zn which will then decay to ^{65}Cu. Gamma spectroscopy will be used to measure the ^{65}Zn that has been created from the ^{64}Zn isotopes by detecting the 1115 keV characteristic γ-ray that results from the decay of ^{65}Zn to ^{65}Cu. Additionally, electron paramagnetic resonance (EPR) measurements will be recorded pre- and post-irradiation to directly measure the ^{65}Cu that has been created in the ZnO crystals as a result of the neutron irradiation.

The final objective of this research is to determine the charge state of the ^{65}Cu atoms introduced as a dopant on the zinc lattice sites. This will be accomplished by EPR spectroscopy. Copper atoms created via transmutation should be in a Cu^{2+} state, but may or may not capture an electron from the material to become Cu^{1+}. Only copper in the Cu^{2+} state will be visible with EPR spectroscopy and if there is no signal then the created copper must have captured an electron.

II. Theory

2.1 Zinc Oxide

2.1.1 Properties and Characteristics

The ZnO samples used in this research are all single-crystals with a wurtzite structure [11] and a density of $5.61\,\frac{g}{cm3}$. Optically, these samples are highly transparent prior to irradiation, though neutron irradiation will create oxygen vacancies that will result in a red or yellow hue [12]. Previous studies have shown that crystal defects will become mobile and begin to migrate to the surface when annealed at 300 ℃ and increased temperature will eventually return the original clarity [12].

As a semiconductor, undoped ZnO is n-type with aluminum, gallium, or hydrogen proposed as the dominant shallow donor [13] and a carrier concentration on the order of $N_D \backsimeq 10^{19}\,cm^{-3}$ [7]. Zn vacancies have been proposed as the dominant acceptor in n-type ZnO with acceptor and vacancy concentrations in good agreement at $N_A \backsimeq N_{Zn_v} \backsimeq 2 \times 10^{15}\,cm^{-3}$ [14]. If true, this makes neutron irradiation of ZnO doubly interesting because Zn vacancies will be created in addition to Cu, both of which may lead to more p-like material.

2.2 Neutron Interaction

Nuclear transmutation occurs when the nucleus of one isotope is converted to another through a nuclear decay. In this research, neutron irradiation is used to create unstable isotopes, heavier by the absorption of a neutron, which can then decay by beta emission or electron capture to another element. NTD, in this instance, means that copper will only form when a ^{64}Zn nucleus captures a neutron to form ^{65}Zn which decays directly to ^{65}Cu. In this way, ^{65}Cu should form only at the ^{64}Zn sites in the lattice.

All of the nuclei in the ZnO crystal can absorb neutrons, but not all of these interactions are particularly important. Many of the nuclei in the crystals do not transmute because they become a heavier, but still stable, isotope of the same element after neutron absorption. For example,

$$^{66}Zn + n \rightarrow {}^{67}Zn + \gamma,$$

also written as ^{66}Zn (n,γ) ^{67}Zn, does not involve a transmutation because the absorption of a neutron in this case leads to ^{67}Zn which is stable. Transmutation doping requires the resultant isotope to be unstable, as is the case for ^{64}Zn, which becomes ^{65}Zn after absorption of a neutron and decays to ^{65}Cu with a half-life of 244 days. This decay is the most important in this research as it is the mechanism by which the copper dopant is introduced into the ZnO crystals. The specific decay paths for ^{65}Zn and other unstable isotopes will be discussed in Sec. 2.3.

These neutron interactions take place in the quantum realm and therefore the process of neutron absorption is probabilistic, which means that many nuclei must be exposed to many neutrons to have even a small percentage of the neutrons absorbed. The neutron absorption cross section is used to represent this probability for absorption and the value for all known elements in the Eagle Picher samples are listed in Table 1. It should be noted that, although oxygen is a major constituent of ZnO, oxygen has been omitted from this table because it is unimportant to this research as shown in Sec. 2.3.1. Additionally, the concentrations for the impurities are based on estimates from similar samples as determined in other studies and do not reflect any measurement of these samples.

Due to the small probability of absorption, a large flux of neutrons is needed and this research will use the reactor at Ohio State University to reach a total neutron flux of approximately $2.1 \times 10^{13} \frac{n}{cm^2 s}$($1.3 \times 10^{13} \frac{n}{cm^2 s}$ thermal). Table 1 provides a

Table 1. Isotopic properties of atoms in Eagle Picher ZnO

Initial Isotope	Concentration $[\# \,/\, cm^3]$	Thermal Neutron Absorption Cross Section [b]	Half-life of Resultant Isotope
^{64}Zn	2.02×10^{22}	0.809	244 d
^{68}Zn	7.80×10^{21}	1.91 (0.07)	57 m (13.76 h)
^{70}Zn	2.57×10^{21}	0.094 (0.009)	2.4 m (3.96 h)
^{63}Cu	7×10^{15}	4.475	12.7 h
^{65}Cu	3×10^{15}	2.31	5.1 m
^{54}Fe	6×10^{14}	2.257	2.7 y
^{58}Fe	3×10^{13}	1.182	44.6 d
^{55}Mn	1×10^{16}	13.87	2.58 h
^{30}Si	3×10^{15}	0.11	2.62 h
^{27}Al	1×10^{17}	0.23	2.24 m
^{69}Ga	6×10^{16}	1.745	21.1 m
^{71}Ga	4×10^{16}	4.845	14.1 h

single value for the neutron absorption cross section which assumes a monoenergetic source of thermal (0.025 eV) neutrons. In fact, the neutrons are of many energies making up a spectrum; however, this spectrum is not well characterized for all of the irradiation facilities at the OSURR. If a neutron flux spectrum were available for each irradiation facility, then it could be paired with the energy dependent cross sectional data, as shown in Fig. 1 for ^{64}Zn, to determine the activation of the ZnO crystals more accurately and more precisely predict the final concentrations of stable isotopes. Such a spectrum does exist for the central irradiation facility and will be used to more accurately predict the activity of the samples irradiated in that facility.

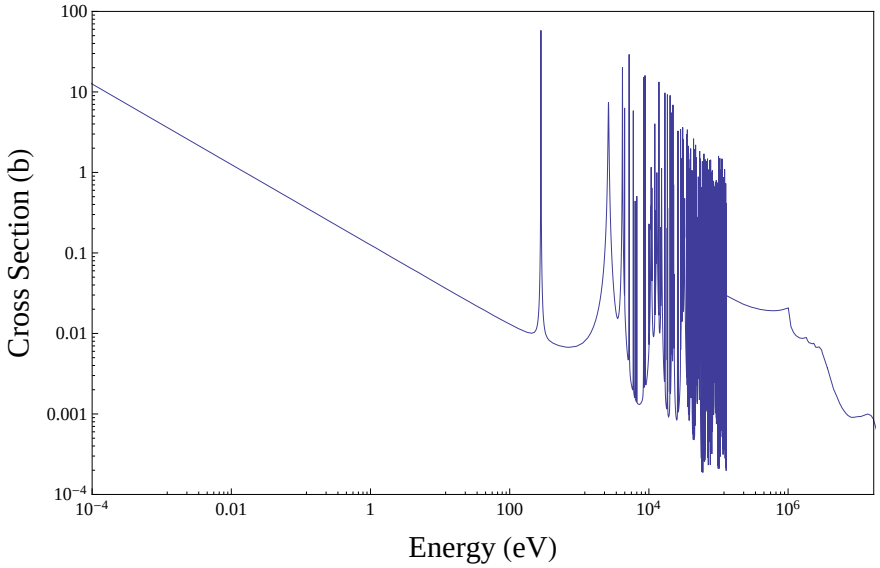

Figure 1. Cross-section data for ^{64}Zn
This is a plot of the energy-dependent cross-section values for neutron absorption in ^{64}Zn. It shows that the thermal region is the most likely to absorb, though the resonance region does provide some strong regions of absorption. This plot is reproduced from the National Nuclear Data Center (NNDC), a product of Brookhaven National Laboratory [15].

Unfortunately, there is currently no data available for neutron spectrum in the thermal column. However, it should be clear from Fig. 1, that the most important region for neutron capture is the thermal region ($\sim$0.025 eV) due to much higher capture cross-sections. The resonance region will provide some additional areas of high capture probability, but lacking a detailed spectrum the assumption will provide an approximate value for the activity of the thermal column samples after irradiation.

2.3 Radioactive Growth and Decay

When the samples of ZnO are irradiated with neutrons the various nuclei in the samples will begin to absorb the neutrons as discussed in the previous section. This absorption will lead to the growth of heavier isotopes and a decay of those that are unstable. This growth and decay process is well understood and easily accounted for using simple nuclear physics. The equations describing this process can be found in

Chapter 6 of Krane [16].

$$R = N_0 \sigma \phi$$

describes the rate of production, R, for a daughter isotope given the number of parent isotopes, N_0, the cross section for neutron absorption, σ, and the flux of neutrons, ϕ. The number of daughter isotopes is then

$$N(t) = \frac{R}{\lambda}(1 - e^{-\lambda t}) \tag{1}$$

where λ is the decay constant, which is Log(2) times the inverse half-life. After irradiation has ceased, the unstable daughter isotopes will continue to decay following a purely exponential decrease in time, as shown in Eq. 2.

$$N(t) = N_0 e^{-\lambda t} \tag{2}$$

The activity of the daughter isotope is simply a product of the number of atoms of a given isotope and their decay constant

$$A(t) = \lambda N(t). \tag{3}$$

The remainder of this section will now consider the various isotopes within ZnO that are of interest. Their interaction with neutrons and subsequent decays will be presented and any γ-rays produced will be identified. Their final electron configuration will be determined to indicate whether or not they are paramagnetic and hence active in EPR spectroscopy.

2.3.1 Oxygen Isotopes

Oxygen has three stable isotopes ^{16}O (99.76%), ^{17}O (0.038%) and ^{18}O (0.204%) [16]. Neutron absorption will create heavier isotopes of oxygen from the stable ones until ^{19}O is created at which point the isotope is now unstable and decays by β^-(100%) to ^{19}F, which is stable. This decay can be to several different excited states of ^{19}F which must then decay to the ground state by releasing a potentially detectable γ-ray. The most intense γ-rays are 197.1 keV (95.9%), 1356.8 keV (50.4%), 1444.1 (2.5%) and 1554.0 keV (1.39%) [17]. The intensity of these gamma rays corresponds to how often they appear from any given decay and are more than 100% because few of the decays in the excited state of ^{19}F are to the ground state, almost all of the decays are cascades passing through the 197.1 keV energy level as shown in Fig. 2.

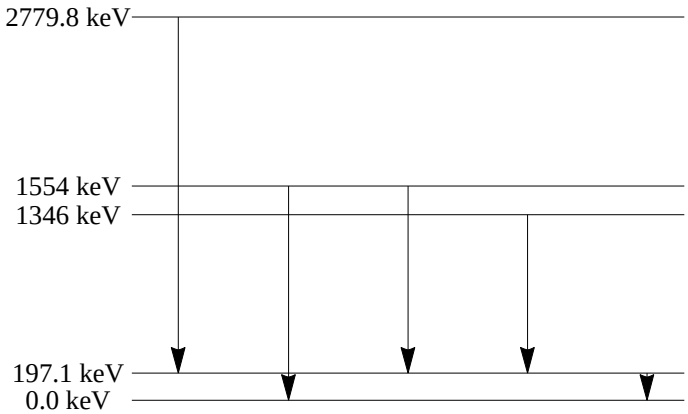

Figure 2. Selected levels of ^{19}O decay scheme
This figure presents some of the transitions possible from the decay of ^{19}O to ^{19}F and subsequent de-excitation of the fluorine nucleus if the decay is not to the ground state. 95.9% of the decays will result in a 197 keV γ-ray emission because very few of the excited states decay directly to the ground state and instead pass through the 197 keV energy level [17].

The electron configuration of oxygen ions in ZnO is [He] $2s^2$ $2p^6$ as it has taken two e^- from a Zn atom. After the ^{18}O nucleus has been transmuted to ^{19}F the fluorine atom maintains a full valence shell and will therefore not alter the carrier

concentration in ZnO. Additionally, the lack of unpaired electrons means it will not be measured by EPR spectroscopy and the strong electronegativity of fluorine [18] means that it cannot easily be made paramagnetic (a requirement for EPR as discussed in Sec. 2.6). Due to the short half-life and low abundance of ^{18}O the γ-rays from the decay of ^{19}O will likely not be visible in the gamma spectrum. The activation and transmutation of oxygen is of little interest to this research for these reasons.

2.3.2 Zinc Isotopes

Zinc has five stable isotopes: ^{64}Zn (48.6%), ^{66}Zn (27.9%), ^{67}Zn (4.1%), ^{68}Zn (18.8%) and ^{70}Zn (0.62%) [16]. Two of the isotopes, ^{66}Zn and ^{67}Zn, are unimportant because, though they are heavier isotopes after absorbing a neutron, they are still stable. The other three are of interest due to their potential to transmute and will be looked at carefully now.

2.3.2.1 ^{64}Zn

The absorption of a neutron by ^{64}Zn leads to the creation of ^{65}Zn and the immediate release of a γ-ray that will not be detected in this experiment because there will not be a detector in the core with the samples during irradiation

$$^{64}Zn + n \rightarrow {}^{65}Zn + \gamma \quad .$$

This resultant isotope, ^{65}Zn, is unstable with a half-life of 244 days and decays via the following three paths to ^{65}Cu as shown in Eqs, 4 - 6.

$$^{65}Zn + e^{-} \rightarrow {}^{65}Cu + \gamma \quad (50.23\%) \tag{4}$$

$$^{65}Zn + e^{-} \rightarrow {}^{65}Cu \quad (48.35\%) \tag{5}$$

$$^{65}Zn \rightarrow {}^{65}Cu + e^{+} + \nu \quad (1.42\%) \tag{6}$$

Eqs. 4 and 5 are electron capture paths, where the ^{65}Zn nucleus captures an inner orbital electron to convert an excess proton to a neutron thereby reducing the Z number of the nucleus and transmuting the nucleus to ^{65}Cu. The first of these electron capture paths occurs 50.23% of the time and results in an excited state of ^{65}Cu which will decay to the ground state by the emission of a 1115.6 keV characteristic γ-ray that will be used to identify ^{65}Zn in sample after irradiation [19]. The second electron capture path decays directly to the ground state and has no associated γ-ray emission. The final decay path is via β^{-}, where an excess proton is converted to a neutron by the emission of a positron and a neutrino. This positron can annihilate in the gamma detector and when it does it will produce two 511 keV γ-rays that will show up in the final spectrum. The decay scheme is shown below in Fig. 3.

The Zn ion in ZnO is Zn^{2+} which means it has an electron configuration [Ar] $3d^{10}$, because the zinc atoms have given up two e^{-} each to bond with the oxygen atoms. After capturing an orbital electron to create ^{65}Cu the electron configuration is that of the original zinc atom reduced by 1 e^{-} which means the copper created in the sample should be Cu^{2+} with an electron configuration of [Ar] $3d^{9}$. This leaves an unpaired electron in the transmuted copper that makes it visible to EPR.

2.3.2.2 ^{68}Zn and ^{70}Zn

^{68}Zn can either become ^{69}Zn or ^{69m}Zn after absorbing a neutron, but then ultimately decays to ^{69}Ga. The meta-stable state will decay directly to the ground state of ^{69}Zn 99.7% of the time via internal transition which will result in a 438.6 keV γ-ray [17]. Once in the ^{69}Zn state, the isotope will decay via β^{-}(99.999%) to the ground state of ^{69}Ga and there is also a small chance (0.03%) for the meta-stable

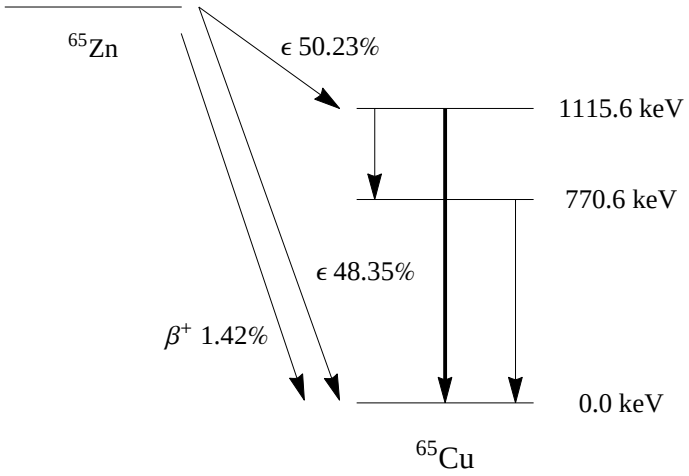

Figure 3. Decay scheme for ^{65}Zn

^{65}Zn decays to ^{65}Cu 100% of the time, but does so via three paths. The first two paths are via electron capture (ϵ). 50.23% of the time this electron capture is to an excited state of copper that then decays via a 1115 keV γ-ray directly to the ground state. There is a small chance (0.0025%) for the excited state of copper to decay to an intermediate energy level, but this signal will likely be lost in the noise. 48.35% of the electron captures are directly to the ground state and result in no γ-ray. Finally, 1.42% of the decays will be β^+ directly to the ground state. This will result in an annihilation peak at 511 keV in the measured gamma spectra for these samples. Produced from data obtained from the Table of Radionuclides [19].

state to decay directly to the ground state of ^{69}Ga via β^- decay [17].

The longer half-life (13.76 hours) of ^{69m}Zn means that ^{69}Zn is being continuously produced for some time after irradiation and the short half-life of ^{69}Zn (56 minutes) means that once it is created it decays quickly with many β-particles emitted. Only the decay from the meta-stable state will be visible to gamma spectroscopy, but the beta emission can be very high early on and is a safety concern for anyone handling the samples.

^{70}Zn also has two possible states after neutron absorption: ^{71}Zn and ^{71m}Zn. Both of these isotopes will decay directly to ^{71}Ga via β^-, though there is an exceedingly small chance ($\leq$0.05%) for the metastable state to decay to the ground state of ^{71}Zn via internal transition and release a γ-ray before decaying to ^{71}Ga [17]. Approximately half of the decays (55%) will be to the ground state of Ga, 32% will be to an excited state that results in the emission of a 511.6 keV γ-ray and the remainder will be to a multitude of other energy levels [17]. The most intense γ-rays resulting from transitions within the ^{71}Ga are 511.6 keV (32%), 910.3 keV (7.8%), 390 keV (3.8%), 121.5 keV (3%) and 1120 keV (2.2%) where the percentages indicate what fraction of decays will emit the specified γ-ray [17]. Due to the short half-life of these isotopes, these γ-rays will not be visible if the sample needs to decay for more than a day to allow for safe handling. They are, however, visible in the 10 minute irradiation spectrum shown in Fig. 6.

One concern with the transmutation of ^{68}Zn and ^{70}Zn is that it leads to gallium which would typically be considered a donor in ZnO when it substitutes for zinc ions. A Ga atom has an electron configuration of [Ar] $3d^{10}4s^24p^1$. In ZnO, two electrons are given to the oxygen ions and one electron can be easily excited into the conduction band. However, the gallium being produced by transmutation comes directly from the zinc atom it is replacing. As discussed before, the electron configuration of Zn in ZnO is [Ar] $3d^{10}$. The transmutation of the nucleus from ^{69}Zn to ^{69}Ga as well as

from ^{71}Zn to ^{71}Ga to involves the emission of an electron in the form of a β-particle but this is from the nucleus and does not involve the orbital electrons. Therefore the gallium produced in this fashion will maintain the original electron configuration and will be Ga^{3+}. This implies that the creation of gallium will not increase the electron carrier concentration in ZnO material.

2.3.3 Impurity Isotopes

2.3.3.1 Copper

Copper is found in Eagle Picher ZnO as an impurity introduced during the CVT growth process [20, 21]. This copper impurity has both stable isotopes, ^{63}Cu and ^{65}Cu, in their natural abundances 69.2% and 30.8% respectively [16]. After absorbing a neutron ^{63}Cu becomes the unstable ^{64}Cu and ^{65}Cu becomes the unstable ^{66}Cu. ^{64}Cu decays via electron capture down to the ground state of ^{64}Ni 43.53% of the time and to an excited state 0.47% of the time, resulting in a 1345.8 keV γ-ray [22]. It can additionally decay via β emission either by β^+ (17.52%) to the ground state of ^{64}Ni or by β^- (38.48%) to the ground state of ^{64}Zn [22]. ^{66}Cu decays by β^- (100%) to ^{66}Zn with 90.8% of the decays being directly to the ground state [17]. An additional 9% of the decays are to an excited state of ^{66}Zn that then de-excite via a 1039.2 keV γ-ray emission [17]. These decay schemes are shown below in Figs. 4 and 5.

As shown in Table 1, copper has a very high cross section for neutron absorption and is easily activated. However, the low concentration of copper in ZnO and the short half-lives of both activated isotopes combined with the relatively long cooling period required after irradiation mean that there will be little opportunity to detect any activated copper via gamma spectroscopy. During a short, 10 minute diagnostic irradiation of ZnO the 1039 keV γ-ray was seen, as shown in Fig. 6, but the 1345 keV γ-ray was lost in the noise due to the low probability (0.47%) of decaying into the excited state that produces it. All other gamma spectra were recorded too long after

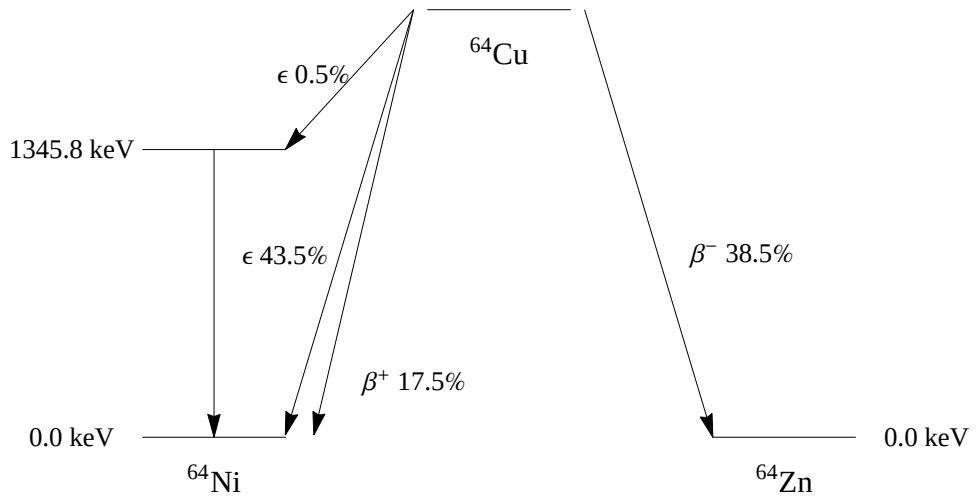

Figure 4. Decay scheme for ^{64}Cu

This plot shows the two decay paths from ^{64}Cu to ^{64}Ni via electron capture (0.5% to an excited state, 43.5% to the ground state) and β^+ emission (17.5%) and one path directly to the ground state of ^{64}Zn via β^- emission (38.5%). The data for this decay scheme comes from the Table of Radionuclides [22].

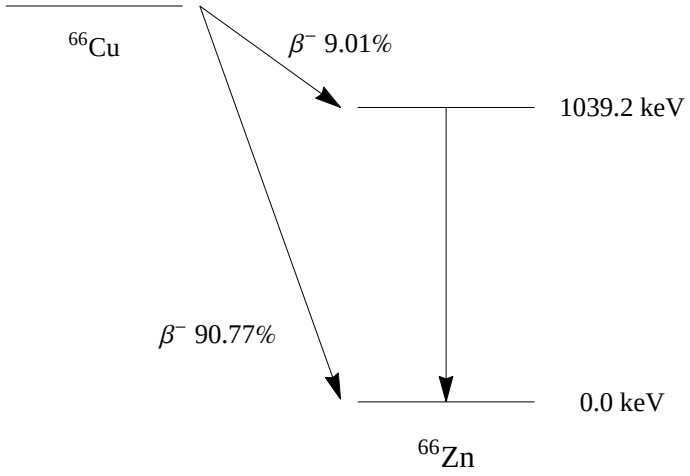

Figure 5. Decay scheme for ^{66}Cu

This plot shows the single decay path from ^{66}Cu to ^{66}Zn via β^-. It also shows that most (90.77%) of the decays will be to the ground state and result in no γ-ray, while 9.01% will transition to an excited state of ^{66}Zn and result in the emission of a 1039.2 keV γ-ray [17].

irradiation for any gamma ray lines corresponding to copper decays to be measured.

2.3.3.2 Effect of Other Impurities

The other impurities in this sample, listed in Table 1, are in such low concentrations that they were not sufficiently activated during any of the irradiations to produce visible signals in the gamma spectra. They were considered in the Mathematica model discussed in Sec. 2.5, and were found to be ultimately inconsequential.

2.4 Gamma Spectroscopy

2.4.1 Gamma Detection

Gamma rays will be detected using a HPGe detector which was selected for its very fine resolution. HPGe detectors have a small band gap (0.7 eV) [23] making it easy for γ-rays to create electron-hole (e-h) pairs as they are absorbed in the detecting material. With only 2.96 eV required to create an e-h pair in HPGe, very small differences in γ-ray energy can be discerned and this is the reason for the fine resolution [23]. This small band gap and energy required to create an e-h pair however makes the detector very sensitive to temperature. To avoid constant creation of e-h pairs due to thermal energy, the detector must be cooled with liquid nitrogen to 77 K.

The e-h pairs created by the γ-rays would just recombine given no stimuli, but in a detector they will be swept apart by an applied electric field. This movement creates a change in the electric field which then produces the signal that will indicate a photon has been absorbed by the detector. The amplitude of the signal is directly related to the number of e-h pairs created and thus the energy of the incident photon.

After the detector, the most important piece of equipment is the multi-channel analyzer (MCA). The MCA breaks the energy spectrum into a set number of bins,

8192 for this experiment, and counts how many times the amplitude of a signal falls into each bin. After calibrating the detector with a known sample the true energy ranges of these bins can be precisely determined and the number of counts can be turned into an energy spectrum that can be analyzed to identify peaks and calculate activities.

2.4.2 Expected Spectral Features

Spectra recorded immediately after irradiation will have many features as shown in Fig. 6. This spectrum is the result of a 10 min irradiation of ZnO performed at the OSURR as part of a diagnostic for reactor safety. However, for longer irradiation times the samples were not safe to handle immediately and the reactor operators requested the samples not be removed from the reactor for at least 6 days. Most of the unstable daughter isotopes had decayed away or were at undetectable levels after this cooling period due to their short half-lives (see Table 1).

Typically, what remained when the samples were safe enough to handle was a small amount ^{69m}Zn and a large amount of ^{65}Zn. The ^{69m}Zn isomer has a 438 keV γ-ray associated with its decay that was undetectable after six days. The only expected measurable decays were due to the decay of ^{65}Zn with a 1115 keV peak corresponding to the electron capture decay as well as a 511 keV annihilation peak corresponding to the β^+ decay as the positron annihilates in the detector and deposits two 511 keV γ-rays.

Two other related features are expected: a Compton edge and a backscatter peak. Both of these features are due to a Compton scattering event in which a γ-ray interacts with an electron and is subsequently scattered. The maximum energy occurs when the photon collides with the electron head-on and is scattered back along its original trajectory. The energy of this resultant γ-ray is given by [23]

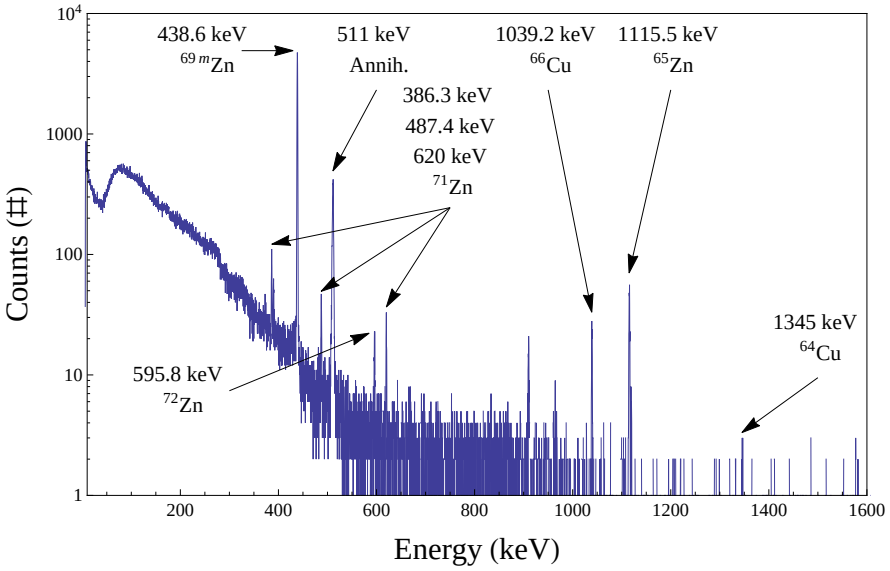

Figure 6. 10-min neutron irradiation of ZnO

This plot shows the spectrum from the 10-min diagnostic irradiation. Due to the short irradiation time this sample could be analyzed and many short lived isotopes were visible. This spectrum shows ^{65}Zn, ^{69m}Zn, ^{71}Zn, ^{72}Zn, ^{64}Cu and^{66}Cu. Two peaks that are not well formed remain unidentified near 909 keV and 964 keV.

$$E_{\gamma'} = \frac{h\nu}{1 + \frac{h\nu}{m_0c^2}(1 - cos\,\theta)}, \tag{7}$$

where $h\nu$ is the energy of the incident γ-ray, m_0c^2 is the rest mass energy of the electron and θ is the angle of scattering for the resultant photon, 90 degrees or π indicates a head-on collision that results in the photon being directed exactly opposite the way it came and represents the minimum energy possible after a Compton scattering event. The Compton edge occurs when a scattered γ-ray escapes the detector material and is no longer recorded in the spectrum. This will then decrease the energy detected by the amount lost which results in a Compton edge located $E_{\gamma'}$ lower than the full energy peak located at 1115 keV. The backscatter peak is the same thing except it occurs in the material surrounding the detector and then the γ-ray enters the detector and is recorded at a separate peak with a lower bound located at the minimum energy of the scattered photon, $E_{\gamma'}$. The relative position

of the Compton edge and backscatter peak are shown in Fig. 7 for a notional full energy peak.

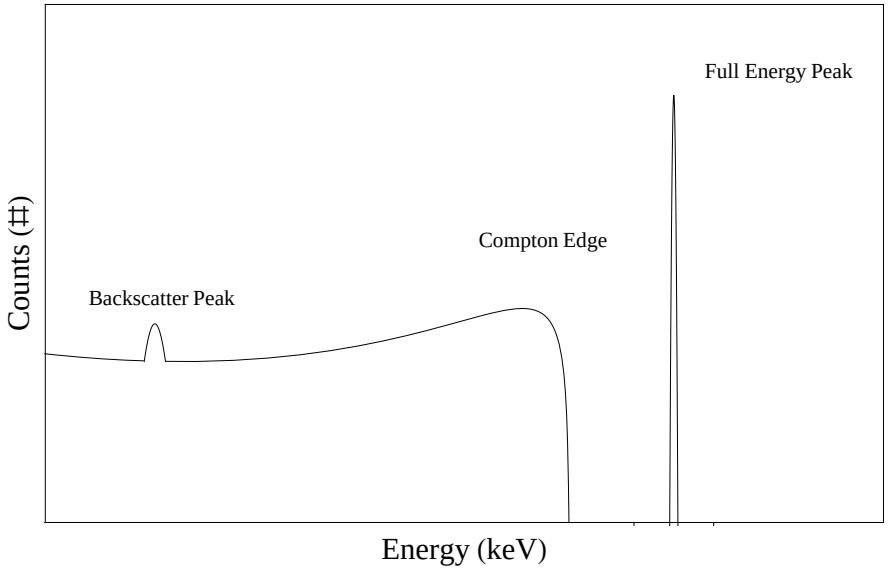

Figure 7. Notional gamma spectrum
This plot shows the positions for the Compton edge and backscatter peak in relation to a notional full energy peak.

2.4.3 Peak Identification and Activity Determination

When analyzing a spectrum, the first step is to identify which isotopes are represented by each peak. This identification is accomplished by finding the centroid of the peak, which corresponds to the energy of the photon detected, and comparing that energy value to a table of principal γ-rays. A principal γ-ray is the most intense γ-ray from a given isotope and is the most likely to be detected. Even though an isotope may decay and emit gammas of many energies, the principal will always be seen and the other gammas can be used to differentiate between two isotopes with similar principal γ-rays.

Finding the centroid is demonstrated on the spectrum from the 10 minute diagnostic irradiation shown in Fig. 6. The peak near 1039 keV, shown in Fig. 8, will be analyzed to find its centroid and this will be used to identify the isotope.

The first step is to subtract off the background noise, which is done by finding the number of counts between peaks that do not correspond to any defined peaks. After the background has been subtracted, the centroid is found by examining the discrete data points [16]

$$centroid = \frac{\sum x_i y_i}{\sum y_i}, \tag{8}$$

where x_i is the energy value for the i-th point and $y_i$is the number of counts for the i-th point (with the background counts subtracted). This bounded region is shown in Fig. 8, with a centroid at 1039.21 keV, corresponding to ^{66}Cu [24].

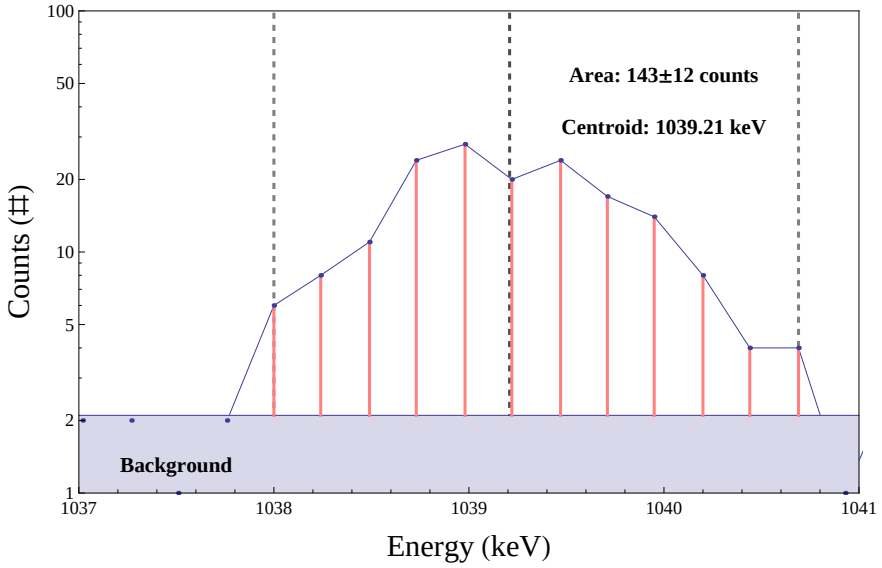

Figure 8. Peak analysis of the 1039 keV region
This plot shows the analysis of the peak in the 1039 keV region. The background count was low, ˜2 counts per channel, and the centroid was found to be 1039.2 keV, identifying the isotope as ^{66}Cu and confirming the presence of copper in the Eagle Picher samples. The total counts in the peak was found to be 143±12, which gives an activity of $0.77 \pm 0.06\,\mu Ci$.

The area under the peak is just the sum of all counts in the region, with the background subtracted. This was found to be 143±12 counts. The error is due to statistical uncertainty and is simply the square root of the total counts. Longer counting would lead to a Gaussian distribution and reduce the uncertainty in the

counts to a very small percentage. The activity is found by

$$A = \frac{counts}{t\,\epsilon_{abs}\,I} \tag{9}$$

where t is the total time for the measurement, ϵ_{abs} is the absolute efficiency of the detector and I is the intensity of the γ-ray as a percentage of total decays that will produce it. The activity of this isotope is found to be $0.77 \pm 0.06\,\mu Ci$.

2.5 Mathematica Model

ZnO may have many zinc and oxygen vacancies as well as impurities unintentionally introduced during the growth of the crystal which must be accounted for because they can also transmute to other atoms, some of which may be undesirable or which might make the gamma spectrum harder to decipher. Therefore isotopes of the highest concentrations (based on published analyses of similarly grown samples [20, 25]) were considered in a model to predict the gamma spectrum resulting from the planned irradiation. Other studies have ignored these impurities and have either focused solely on the main isotopes of interest [2] or included the isotopes of Zn and O, but no others [5]. This work will consider all isotopes (Al, Ga, Si, etc) and will consider the effect of their transmutation.

2.5.1 Assumptions

The model was written as a feasibility study to determine three things: the activity of a sample after irradiation, the amount of ^{65}Cu created as a function of time and how easy it would be to identify the peaks in the gamma spectra at various times after irradiation. The model was able to address these areas, though some assumptions were necessary to make the calculation.

The first assumption was that only thermal neutrons would be captured and that

these were monoenergetic at 0.025 eV with a flux of 1.3×10^{13} n cm^{-2}s^{-1} for samples in the CIF and 4.3×10^{11} n cm^{-2}s^{-1} for samples in the TC [26]. The thermal fluxes came from the OSURR datasheet but the width of the "thermal" region was not described. This assumption was valid because the highest probability of absorption is in the thermal region, as shown in Fig. 1, and this should provide the bulk of the transmutation interactions. However, there was enough data available for the CIF that an actual neutron flux spectrum could be paired with the ^{64}Zn neutron capture cross-section to allow for more accurate prediction of the counts for that isotope. Unfortunately, there was no energy dependent cross-section data available for the ^{69m}Zn isomer.

The second assumption was that the reactor would be operated continuously, which is not correct. In reality the reactor is run at most 7 hours a day and usually only a few days a week due to limited manpower. However, this assumption is shown to be valid by using the model to find the concentration of ^{65}Zn after 20 hours of irradiation from both an intermittent and a continuous irradiation. The two operating methods end up giving essentially the same concentration of ^{65}Zn, as shown in Fig. 9, with the continuous irradiation being slightly higher by 0.2%.

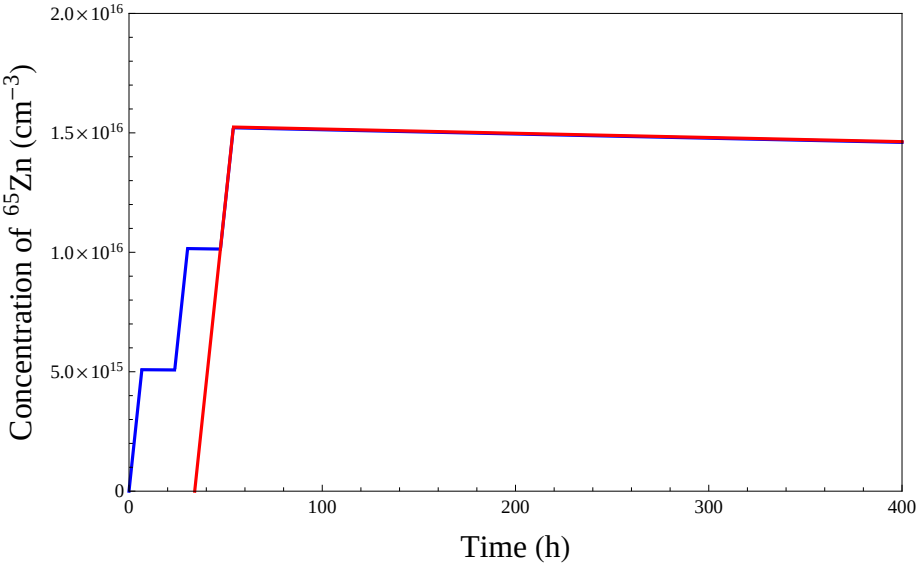

Figure 9. Comparison of continuous and intermittent irradiation
This plot compares the final concentration of ^{65}Zn after 20 hours irradiation operated both continuously (red) and intermittently (blue). The continuous operation is timed such that its irradiation concludes at the same time as the intermittent operation. The two methods produce the same concentrations of ^{65}Zn, with the continuous irradiation being slightly higher by 0.2%.

2.5.2 Predicting the Spectrum and Calculating Activity

The first step in the model is to set the variables required to make the calculations. This includes the reactor flux, the time of irradiation, how long after irradiation for gamma measurements, the mass of the sample and the resolution and efficiency calibrations for the detector that will be used. Stored in the code are the concentrations of all isotopes in Eagle Picher ZnO that become unstable when absorbing a neutron, the neutron absorption cross-section (at 0.025 eV) for these isotopes and the half-lives of the unstable isotopes created.

When the code is executed, it uses the values entered along with the stored values to solve Eq. 1 in time during the irradiation and Eq. 2 in time after irradiation. The activity is calculated by multiplying these two equations with the decay constant, as in Eq. 3, and making a piecewise solution with the time of irradiation marking the boundary between the two solutions. Since the activity is the number of decays

per second, the number of transmuted atoms can be found at any point in time by integrating this piecewise solution for activity in time from zero to the time of interest.

The gamma spectrum is predicted by considering the activity of each of the isotopes and the intensities of the γ-rays that result from their decays. This is turned into the number of counts detected by

$$counts = \epsilon_{abs} A t I ,$$

where ϵ_{abs} is the energy dependent absolute efficiency of the detector and describes what fraction of all decays will be absorbed by the detector for a specific geometry, A is the activity of the sample in decays per second, t is the total time of the measurement, and I is the intensity of the single γ-ray being considered. This is done for all of the γ-rays associated with each decay to determine how many counts there will be at any given energy level.

Once the counts are known, a Gaussian, centered at the energy level of the γ-ray, is plotted using the energy dependent resolution from the detector's calibration to determine the σ value and the counts to fix the area. This will not be an exact prediction of the spectrum, because it assumes the total counts represent the area under a Gaussian. Instead, the counts are actually distributed discretely and any Gaussian that bounds them will have an area larger than the sum of the counts contained. However, for predictive purposes this method will suffice.

The predicted gamma spectrum measured 6 days after irradiation for the short, 5-hour irradiation in the CIF is shown in Fig. 10. Only three full energy peaks are plotted in this prediction. If the calculations are correct and the assumptions valid, then the spectra from the irradiated samples should be easily identifiable.

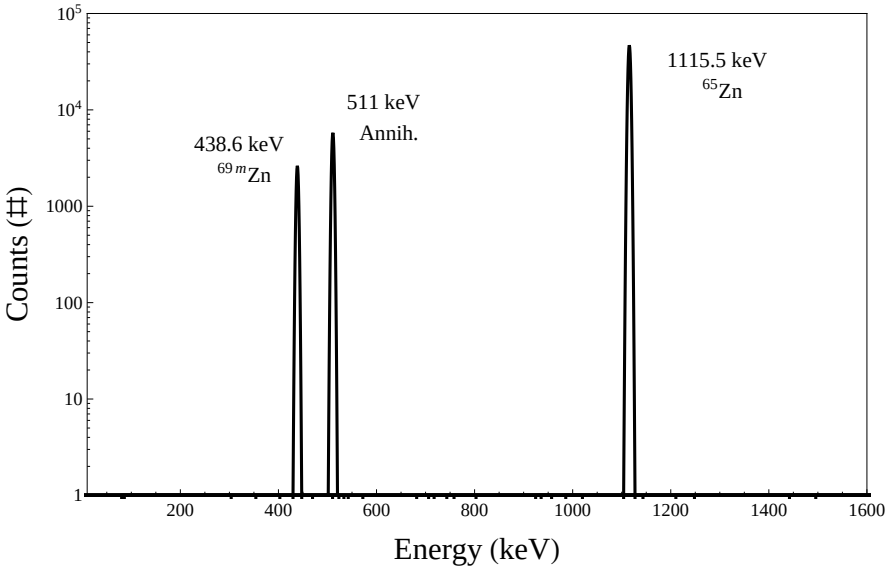

Figure 10. Predicted gamma spectrum after 5 hours of irradiation in the CIF This graphics is a representation of the predicted gamma spectrum for Eagle Picher ZnO after 5 hours of irradiation in the CIF. It is assumed that the wait time will be approximately 6 days to allow the samples to cool. In this time, almost all of the short-lived isotopes will have decayed away and only ^{69m}Zn and ^{65}Zn will be detectable. The 20-hour irradiation will require a longer time to cool and thus the ^{69m}Zn will no longer be detectable and only ^{65}Zn will remain.

The model was useful in determining that this experiment was not only feasible, but that the gamma spectrum would be simple to analyze because only one or two isotopes would be present depending on how quickly after irradiation the spectrum could be recorded. The Gaussian functional fits provide a notional spectrum but no metric for comparison of the model to the measured data. It would be better to compare the counts predicted to those measured, which relate directly to the activity of the sample. These values are listed in Table 2 and will be compared to the measured values in Chapter IV. Samples are labeled with the following scheme: 'S' indicates a short irradiation (5 hours), 'M' indicates a long irradiation (20 hours) all cut from a single crystal, and 'H' indicates larger samples that also received a long irradiation (20 hours) but were either from a different crystal or were produced via hydrothermal growth as opposed to CVT.

Table 2. Predicted peak counts and total activity

Sample	Counts 438.6 keV	Counts 511 keV	Counts 1115.5 keV	Total Activity
S1	14756±121	28220±167	251055±498	88.2 μCi
S2	1535±39	3637±60	32352±180	11.5 μCi
M3	0	5155±72	42242±206	68.5 μCi
M4	0	7007±84	57421±240	93.2 μCi
M5	0	3252±26	26129±162	3.3 μCi
M6	0	2934±54	23578±154	1.4 μCi
H1	0	12565±118	102957±337	167.0 μCi
H2	0	5829±76	47772±218	77.5 μCi
H3	0	20951±152	171674±435	278.5 μCi

The purpose of the model was to complete a feasibility study for this experiment. Specifically, to find out whether the gamma spectrum would be decipherable and to determine, roughly, the activity of the samples after irradiation for safety and transportability. Ultimately, the model served this purpose well and was able to determine that the samples would be at safe activity levels within a few days after irradiation and that the gamma spectrum should be clear and easy to read without any signals stemming from impurities in the samples.

2.6 EPR Spectroscopy

2.6.1 Zeeman Effect

Dutch physicist Pieter Zeeman observed, in 1896, that atoms placed in an external magnetic field and subsequently excited would de-excite and the spectral lines corresponding to this de-excitation would be split into multiple lines when compared to the same excitation and de-excitation with no magnetic field applied [27]. In the absence of a magnetic field, all states with the same value for the quantum number n are degenerate, but an external magnetic field forces different energies to be associated with discrete values of angular momentum [28]. Electrons, having a spin of $\pm 1/2$, will have minimal energy when they are aligned parallel (m_s = - 1/2) to

the magnetic field and maximal energy when they are aligned antiparallel ($m_s = +$ 1/2) [29].

The primary energy difference detected in EPR spectroscopy is due to this interaction of unpaired electrons with the external magnetic field [29]. The energies of the two states are determined by the strength of the magnetic field

$$E = g\,\mu_B\,B_0\,m_s = \pm\frac{1}{2}\,g\,\mu_B\,B_0\,, \tag{10}$$

where g is a proportionality constant known as the g-factor, μ_B is the Bohr magneton, and B_0 is the strength of the applied magnetic field [29]. The energy difference between the two states is simply [29]

$$\Delta E = h\nu = g\,\mu_B\,B_0\,. \tag{11}$$

The value $h\nu$ is the energy required for an external electromagnetic wave, oriented such that its own magnetic field is perpendicular to the applied magnetic field, to excite the electron from the m_s = - 1/2 to the higher energy m_s = + 1/2 state [30].

This interaction can be used to generate a spectrum in one of two ways. The first is to apply a constant magnetic field and vary the frequency of an electromagnetic wave. As the frequency is increased it will eventually satisfy the requirements of Eq. 11 and the electron will be excited into the higher energy state [29]. This method does not work well in practice, however, because the electromagnetic waves used are microwaves and the geometry of the cavity is specifically design for a single frequency; this method would require a new geometry for each change in frequency [30]. The second method is to hold a steady microwave frequency and vary the strength of the magnetic field. In the same way, at some field strength Eq. 11 will be satisfied and the electron will be excited into a higher energy state [29]. This is the method used for most EPR spectrometers.

The EPR spectrum is created by observing the microwave energy absorbed by the material when the magnetic field passes through "resonances". When magnetic field strength satisfies Eq. 11, some of the microwave radiation will be absorbed in the excitation of the unpaired electron and the microwave power reflected from the microwave cavity will change. As the magnetic field continues to increase in strength the microwave radiation (being held constant) will no longer be resonately sufficient to excite the electron [30]. This rise in absorption is what generates the signal in the EPR spectrum and is shown in Fig. 11.

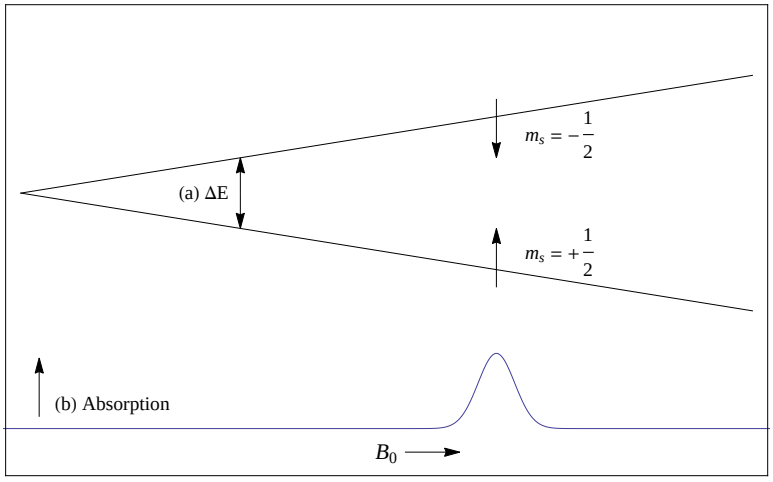

Figure 11. Zeeman effect
This graphic demonstrates the Zeeman effect and how it can be used to produce a spectrum. Part (a) indicates the splitting of the energy levels due to the application of the external microwave radiation, the separation between the two lines indicating the energy required to transition from one state to the other. The trace (b) indicates the amount of the microwave signal that is being absorbed, as the magnetic field strength, B_0, is increased. Produced from data obtained from Bruker EMX User's Manual [29].

2.6.2 Hyperfine Splitting

Additional splitting occurs as a result of the interaction of the magnetic moment of the nucleus with the magnetic moment of the unpaired electron [31]. This leads to four energy levels for a spin 1/2 nucleus (like hydrogen), but only two transitions are

allowed [31]. The effect on the EPR spectrum is that the signal due to the Zeeman effect splits into multiple signals by

$$\#\ of\ hyperfine\ lines\ =\ 2\,I\ +\ 1\,,$$

where I is the spin of the nucleus [29]. The splitting is demonstrated in Fig. 12. Copper, where both ^{63}Cu and ^{65}Cu have a nuclear spin of 3/2, will have four evenly spaced resonances. Also shown in this figure is the conversion to the first derivative of the absorption signal, which is which is the way spectra actually appear, due to an applied magnetic-field modulation that greatly increases the sensitivity of the apparatus [30].

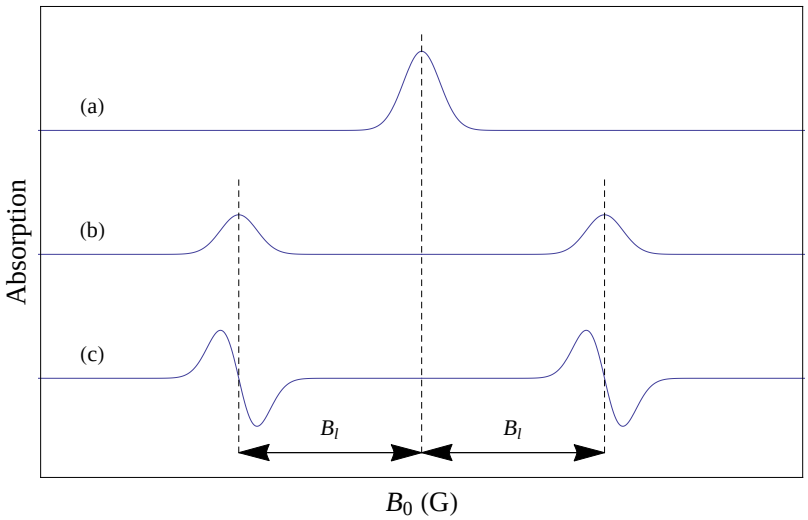

Figure 12. Hyperfine splitting effect
This plot shows the effect hyperfine splitting has for a 1/2 spin nucleus. The first trace (a) indicates the absorption signal that would be detected without hyperfine splitting. The second (b) demonstrates how the interaction of the electron with the nucleus splits the signal in two signals, each shifted from the original center by $\pm B_l$, the magnetic field exerted on the electron by the nucleus. The third trace (c) shows the final form of the signal which is the first derivative of the absorption signal recorded in trace (b). Produced from data obtained from Bruker EMX User's Manual [29].

2.6.3 EPR Spectrometer System

The basic components for EPR spectroscopy are the microwave bridge, the EPR cavity and the large magnet to apply the variable magnetic field. The microwave bridge consists of a microwave source and waveguide which directs microwave radiation to the sample in the EPR cavity. The microwave bridge has an attenuator to allow control of the power of the microwaves emitted, but the frequency of the microwave is fixed. These microwaves interact with the sample material in the EPR cavity and are reflected back into the microwave bridge, through a circulator and directed to a detector which measures the amount of energy reflected back from the sample. The amount of reflected microwave power will increase during a resonance as the cavity becomes slightly mismatched. Control hardware and a computer station display this absorption data as a spectrum that can then be interpreted to identify properties and structure of the sample material. [29]

2.7 Selecting Samples for NTD

One of the difficulties in using NTD is to select a starting material that will transmute to a desired element. Typically, the transmutations possible are due to β-decay or electron capture, which means that the number of protons can only be increased or decreased by one. For semiconductor materials this may be a profitable endeavor and in fact has been used commercially to dope silicon with phosphorus [4]. The difficulty, though, is that each isotope of an element may decay differently (even a single isotope may decay in several ways to multiple stable elements) and maybe only some of these transmutations are desirable. This problem is compounded when the semiconductor is a III-V or II-VI material which will have two constituent elements each having a variety of isotopes that can decay in different ways to different elements.

When considering a semiconductor for NTD, all of the stable isotopes of each

element must be identified. The abundance of each isotope, combined with the cross-section for neutron absorption, will determine the concentration of unstable isotopes created; isotopes that are stable after neutron absorption can be neglected as they will not transmute. The decay scheme for each of these unstable isotopes can then be used in conjunction with their half-lives to determine the concentration of all the stable products after irradiation. In this way, the most significant dopant can be determined and properties of the semiconductor after NTD can be predicted. This analysis will give a very rough prediction, which may be enough to determine whether irradiation and laboratory measurements are warranted or undesirable.

The samples used in this research were ultimately pure enough that the impurities had very little effect, but they should still be considered as they might lead to unwanted elements that could either work counter to those introduced via NTD or may increase the activity in unforeseen ways.

This technique could be explored for optical materials, which also require doping, but it would only be worthwhile to explore if a potential dopant element was directly next to one of the bulk material elements on the periodic table. For example, YAG is a popular material for lasers but it is typically doped with rare earth elements like Nd. No amount of neutron irradiation will be able to produce Nd within a YAG samples, however, some of the Y could be transmuted to Zr and if this provides any benefit to the optical material then it would be worthwhile to investigate NTD of YAG.

III. Experiment

3.1 Material

The ZnO samples used for the irradiations were mostly from Eagle Picher although two samples, one each, from Airtron and Tokyo Denpa were used in the long irradiation. Prior to irradiating the samples for the short irradiation, it was known that the pieces were too large for EPR but it was decided that they could be cut to size after irradiation. This was ultimately a needless hazard and the pieces should have been cut prior to irradiation to avoid inhalation of activated dust that could have been created during the cutting process. Instead of precisely cutting the samples, it was determined to be safer to scribe the irradiated samples with a diamond-tip cutting tool and delicately break off a piece that would fit in the EPR apparatus.

The lesson was learned for the long irradiation and the samples were cut to an appropriate size for EPR measurement (approximately $2\times4\times0.5$ mm^3) prior to irradiation, thus mitigating any risk of radioactive dust being inhaled. Samples M1, M2, M3, M4, M5 and M6 were all cut from the same source a thin single-crystal sample from Eagle Picher referred to as Crystal C. Samples H1, H2 and H3 did not require cutting as they were already sized for EPR and were all from separate crystals. All of the samples for the short irradiation are listed in Table 4, while the samples for the long irradiation are listed in Table 5.

There was no special treatment or cleaning performed on any of the samples prior to irradiation, and all but one were in their as-grown configuration. Two samples (M2 and M3) were characterized with EPR prior to irradiation with measurements taken both before and after a 900 °C anneal in air, the results are discussed below in the procedure for the long irradiation. Samples M1, M2 and the remainder of Crystal C were retained as reference samples and were not irradiated. The remaining crystals

were all irradiated as described below.

3.2 Reactor Facility

The reactor used in this research is the Ohio State University Research Reactor (OSURR) in Columbus, OH. This reactor is not run continuously and is limited to approximately 6-7 hour runs, about 3 days a week though more might be possible. It was shown that this intermittent operation does not greatly affect the activation of the ZnO samples in Sec. 2.5. The OSURR is a pool-type reactor that currently operates at a maximum power of 450 kW and has several irradiation facilities to provide a variety of fluxes for neutron irradiation [26]. The central irradiation facility (CIF) and the thermal column (TC) are the two facilities used in this experiment, but all available irradiation facilities are shown and summarized below in Table 3. All of the fluxes listed were based on the reactor operating at 450 kW, as it was for this experiment, and should be linearly scaled to whatever power the reactor is operating at as a fraction of 450 kW.

Table 3. OSURR irradiation facilities

Irradiation Facility	Size [26]	Total Flux (n $cm^{-2}s^{-1}$) [26]	Thermal Flux (n $cm^{-2}s^{-1}$) [26]
Central	1.3 in.	2.1×10^{13}	1.3×10^{13}
Auxiliary	2.5 in.	8.4×10^{12}	4.1×10^{12}
Peripheral	2.5 in.	5.0×10^{12}	3.0×10^{12}
Pneumatic Transfer	2.5 in.	2.9×10^{12}	1.9×10^{12}
Thermal Column	4 in.	6.1×10^{11}	4.3×10^{11}

The fluxes indicated are for operation at 450 kW and scale linearly with operation power. These values were reported by the OSURR fact sheet and were not measured in this experiment.

The CIF uses a small quartz basket to lower a sample down a 1.3-inch interior diameter tube into the center of the reactor. This area provides the maximum total flux available with $\phi_{total} = 2.1 \times 10^{13} \frac{neutrons}{cm^2 s}$ and also the highest thermal flux at $\phi_{thermal} = 1.3 \times 10^{13} \frac{thermal\,neutrons}{cm^2 s}$, based upon the reactor operators' provided

data [26]. The TC irradiation site is on the side of the reactor and consists of a series of graphite stringers that are used to moderate the neutrons. To irradiate the samples in the TC one of the central graphite stringers must be removed and the sample can be attached to the back of the stringer with tape if the sample is thin enough that the stringer can be replaced without crushing the sample and the irradiation is short enough that the tape does not lose its adhesivity or else a stringer with a recess must be used in its place to accommodate the sample. This facility has a much lower, but more thermalized, flux with $\phi_{total} = 6.8 \times 10^{11} \frac{neutrons}{cm^2 s}$ and $\phi_{thermal} = 4.8 \times 10^{11} \frac{thermal\,neutrons}{cm^2 s}$ [26]. Taping the samples to the reverse of the stringer ended up being the best mounting strategy for a 20 hour irradiation of the ZnO crystals.

One of the benefits of using the OSURR is the proximity to AFIT and the history of cooperation on projects. This history allows AFIT students to "piggy-back" on reactor time as long as it does not interfere with the main experiment being performed. Originally, it was hoped that approximately 100 hours of irradiation could be accomplished in this way and the auxiliary and peripheral irradiation facilities were considered possible locations for the ZnO crystals. This research, however, came up during a dry spell for the OSURR and there were no opportunities to "piggy back" on any full power runs which meant that the irradiation time had to be paid for and limited to 20 hours.

Finally, the pneumatic transfer irradiation facility, or the rabbit tube as it is affectionately called, was used for a very short (10 minute) irradiation to allow the reactor operators to determine what isotopes would be created due to the impurities in the sample as well as better predict what the final activation of the longer irradiations would be. This spectrum is shown in Fig. 6 and discussed in the previous chapter. With a total flux of $\phi_{total} = 3.2 \times 10^{12} \frac{neutrons}{cm^2 s}$, the rabbit is comparable to the core, though lower by an order of magnitude. The rabbit uses a pneumatic transfer tube

to propel a sample towards the core of the reactor and has a timer that can be set to determine how long a sample will be irradiated before it is shot back. When the sample returns it is deposited into a lead box where it is allowed to cool before being removed and handled. This irradiation facility allows for quick irradiations of precise durations, but can be harsh on the samples. The ZnO sample used in this calibration was inside a plastic bottle with cotton balls to protect the crystal from the shocks of being shot back and forth but was still broken. Fortunately most of the sample was still in one piece and there was no harm done to the experiment, but this irradiation facility should be used with caution if the samples are delicate.

3.3 Equipment

3.3.1 Canberra High-Purity Germanium (HPGe) Gamma Detector

Canberra HPGe detectors, cooled with liquid nitrogen, were used to collect the gamma spectra from the samples after irradiation. The spectra were recorded at both OSU and AFIT, though there were issues with the calibration of the AFIT detectors as discussed in Section 3.5. Both detectors showed identical spectra, but the AFIT measured spectra were slightly offset due to the difficulty in calibration.

3.3.2 Bruker EPR Spectrometer

A Bruker EPR spectrometer owned by AFIT was used to collect the EPR spectra. This setup uses an external liquid helium tank and a pump to control the flow of He gas to keep the samples cooled to temperatures as low as a few kelvin. Additionally, a laser operating at 442 nm is used to excite the atoms in the sample, altering signals and making some previously invisible features visible.

3.4 Irradiation Procedure

This research was accomplished with a short and a long irradiation. The short irradiation had two samples of Eagle Picher material placed, one each, in the CIF and TC for 5 and 7 hours of irradiation, respectively. The long irradiation also made use of Eagle Picher material but additionally used two samples from Tokyo Denpa and Airtron. The CIF and TC were the only irradiation facilities used for this research.

3.4.1 Short Irradiation

The initial radiation was accomplished as part of a laboratory assignment to understand the interaction of material with neutron irradiation. The two samples were pieces that were either irregularly shaped or had broken off of a larger sample and are summarized below in Table 4. Sample S1 was placed in the CIF while OSURR was operated at 450 kW for five hours and received a total fluence of 3.7×10^{17} neutrons cm^{-2} (2.3×10^{17} thermal neutrons cm^{-2}). Sample S2 was placed in the TC during the short irradiation, but also received two additional hours; one at 450 kW and one at 350 kW for a total fluence of 1.5×10^{16} neutrons cm^{-2} (1.1×10^{16} thermal neutrons cm^{-2}).

Table 4. ZnO samples used for the short irradiation

Sample	Mass (mg)	Location	Source	Growth
S1	182.6±0.1	CIF	Eagle Picher (Crystal A)	CVT
S2	424.6±0.1	TC	Eagle Picher (Crystal B)	CVT

After a period of 6 days the short-lived isotopes had decayed away and the samples were cool enough to examine. They were removed from the reactor and immediately measured on the HPGe detector. After recording their activities, the samples were

transported back to AFIT and stored in a lead pig until they were transported to the EPR laboratory for EPR measurements.

3.4.2 Long Irradiation

Prior to the long irradiation, samples of ZnO were cut to an appropriate size for EPR measurements (approximately 2mm×4mm×0.5mm) and were then weighed for later identification. In addition to the Eagle Picher material, samples from Tokyo Denpa and Airtron were also irradiated as a comparison between the CVD and hydro growth method. All of the samples for this irradiation are listed below in Table 5.

Table 5. ZnO samples used for the long irradiation

Sample	Mass (mg)	Location	Source	Growth
M1	not meas.	Ref.	Eagle Picher (Crystal C)	CVT
M2	not meas.	Ref.	Eagle Picher (Crystal C)	CVT
M3	35.9±0.1	CIF	Eagle Picher (Crystal C)	CVT
M4	48.8±0.1	CIF	Eagle Picher (Crystal C)	CVT
M5	42.5±0.1	TC	Eagle Picher (Crystal C)	CVT
M6	17.9±0.1	TC	Eagle Picher (Crystal C)	CVT
H1	87.5±0.1	CIF	Eagle Picher (Crystal D)	CVT
H2	40.6±0.1	CIF	Tokyo Denpa	Hydrothermal
H3	145.9±0.1	CIF	Airtron	Hydrothermal

Samples M1 and M2 were reserved as reference samples and were not irradiated. EPR spectra were recorded for samples M2 and M3 prior to irradiation in both an as-grown state and after being annealed in air at 900 °C. Prior to the anneal, neither sample showed any copper signal in the spectra, as shown in Fig. 13. After annealing in air and then exposing the samples to a 442 nm beam, both samples show copper signals, as shown in Fig. 14. These signals have been identified in the literature as Cu^{2+} ions [20] and are not visible without the laser light.

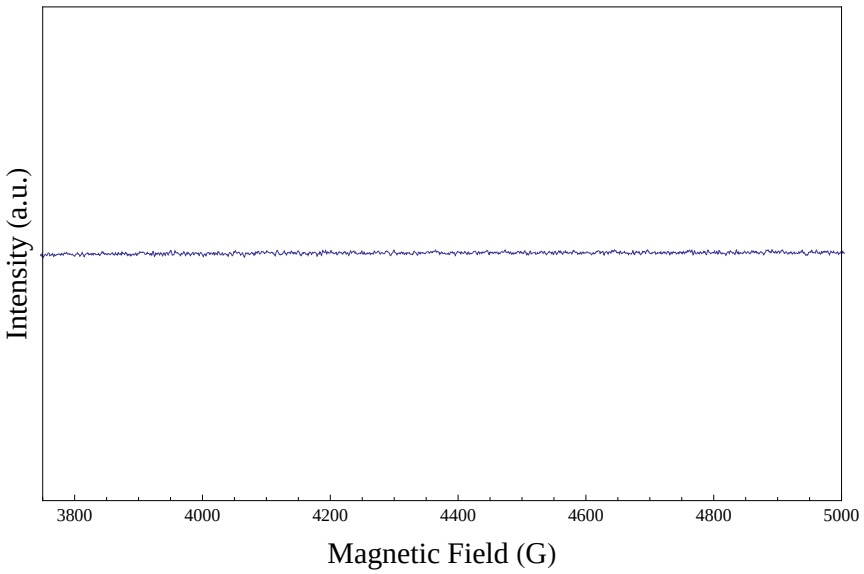

Figure 13. Copper region EPR spectrum for as-grown sample M2

The EPR spectrum for the as-grown Eagle Picher material shows no signals prior to an anneal/illumination in the Cu region. Copper is known to exist as an impurity unintentionally introduced during the growth of this material [20], but it currently exists in a non-paramagnetic state and is not visible to EPR.

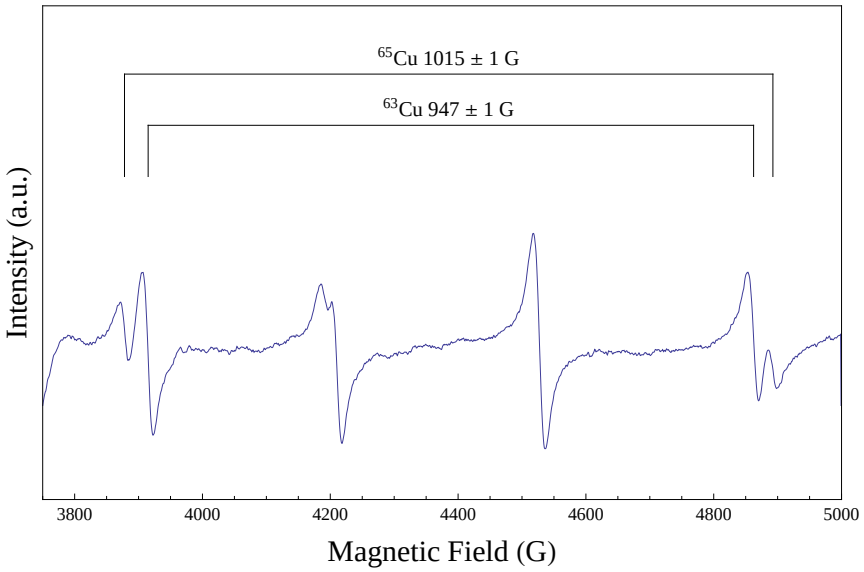

Figure 14. Copper region EPR spectrum for sample M2 after annealing in air

After annealing in air at 900 °C and exposure to 442 nm light, the sample shows a clear signal indicating copper is present. The two outermost signals have two peaks that indicate the presence of both isotopes of Cu. The smaller of the peaks indicates the least abundant isotope ^{65}Cu and the larger indicates the more abundant ^{63}Cu. The separation for ^{65}Cu was measured to be 1015±1 G and ^{63}Cu was found to be 947±1 G. The innermost set of signals do not have any isotopic information because the individual signals overlap and are not distinguishable.

The reason copper is not initially visible to EPR is not entirely known, but one theory is that a complex defect forms near the copper atoms, possibly involving an OH ion, that does not behave paramagnetically. When the sample is annealed in air, the defect is changed, i.e., the hydrogen is driven away leaving copper atoms in a Cu^{+1} state, which has an electron configuration of [Ar] $3d^{10}$. In this state there are no unpaired electrons and the copper present is not paramagnetic and cannot be detected by EPR [20]. When the sample is exposed to laser light at low temperature, weakly bound electrons can be excited to the conduction band leaving behind Cu^{+2} , with an electron configuration of [Ar] $2d^9$, which is now paramagnetic and detectable.

Four lines appear in the EPR spectrum due to the hyperfine interaction of the unpaired electron with the copper nucleus. Additionally, the two isotopes of copper can be seen in the outer set of peaks, the taller peaks indicates ^{63}Cu which is more abundant naturally (69%) and the smaller peaks indicate ^{65}Cu which is less abundant (31%). The neutron irradiation of ZnO should only result in an increase in ^{65}Cu which should eventually result in reversal in the peak amplitudes. The exact position of each peak is determined by instrument settings (e.g., microwave frequency and exact alignment of the crystal with the magnetic field perpendicular to the c-axis) that can vary from measurement to measurement, but the relative distance between the peaks is a constant. The distance between the peaks was determined to be approximately 1014±1 G for ^{65}Cu and 947±1 G for ^{63}Cu, which will be used later to confirm the isotopes detected in EPR spectra. The two isotopes are not discernible in the two inner signals because there is not enough separation and the signals overlap.

Once the pre-irradiation measurements were recorded, the samples were irradiated in the CIF for 20 hours (M5 and M6 were placed in the TC). The crystals cooled for 11 days before they were removed from the reactor and their gamma spectra measured.

3.5 Gamma Spectroscopy Procedure

The gamma spectra were recorded at both OSU and AFIT, using similar methods. The first step was to set the proper calibration. The OSU detectors were already calibrated for all of the different geometries, but the AFIT detectors needed to be re-calibrated. This calibration was accomplished with a multi-nuclide planchette of known nuclides and activities. The planchette was placed in the same configuration as the sample and counts were measured for several minutes to allow for good statistics. After the counting was complete the peaks were identified by the software and matched to the data file accompanying the planchette to match peaks and determine the energy and efficiency calibrations. This was the absolute efficiency and accounted for the solid angle and any other geometries within the detector as long as the sample was placed in the same position.

After this calibration, the samples were placed into the detector and counts were recorded for as little as a minute to as much as thirty minutes to minimize the error in measurement. The goal was to achieve at least 10,000 counts under the peaks which would give the activity with a statistical error of $\pm 1\%$. The samples from the TC were very simple to count and could be placed directly on the detector head and provide clear signals and strong peaks with very little dead time. The CIF samples, however, were hot enough that the samples had excessive amounts of dead time. Multiple lead attenuation disks were used to diminish the intensity of the radiation reaching the detector head, but the resulting spectra were not very useful, as will be discussed in the results and analysis section.

Calibrating for a new geometry also turned out to be difficult because the calibration source was overly attenuated and had to be measured for an hour to obtain any significant peaks. Even after 1 hour, only the higher energy peaks were visible since the lower energy photons could not pass through the attenuation disks. As

a result, the energy calibration could only be performed for the high energy peaks which meant that the low energy spectrum was unreliable and could not be fit. Thus, the activity of the ZnO samples could not be accurately measured. Additionally, the CIF samples had excessive dead times ranging from 37% to 67%. Ultimately, due to these issues, the spectra recorded at OSU were much more accurate and were the ones chosen for analysis in the following chapter.

3.6 EPR Spectroscopy Procedure

The EPR spectra were recorded at AFIT with the assistance of Dr. Larry Halliburton and Capt Shamaun Holston. After irradiation, the samples were stored in a lead pig which was placed inside a lead box. Despite having relatively low levels of radioactivity, the samples were handled with care and personal dosimetry was worn whenever handling was required. Additionally, a handheld detector was kept in the lab at all times to monitor the dose rate from the samples. Samples were removed, one at a time, from the lead container and inserted into the EPR cavity and aligned relative to the magnetic field to produce the strongest signals possible.

To record the spectra from the substitional Cu^{2+} ions, the sample was cooled to approximately 6-7 K and oriented with the c-axis perpendicular to the static magnetic field. The magnetic field strength was then swept from 3750 G to 5000 G, where the copper region is known to be in ZnO [20]. Sixteen measurements were added together to increase the signal-to-noise ratio by a factor of four. Spectra were recorded both with and without laser light on the samples to determine whether any additional Cu^{1+} was in the sample that could be pumped to Cu^{2+}.

After recording all spectra for a given crystal, the sample was removed from the apparatus and returned to the lead pig and lead storage box before the next sample was removed and taken to the lab for measurement. This was done for all samples.

IV. Results and Analysis

4.1 Gamma Spectroscopy

Both of the irradiations, long and short, had similar gamma spectra. There were no major discrepancies in the spectra from either irradiation, but the short irradiation samples were able to be pulled from the reactor sooner due to being less activated which meant that an additional peak was visible in the spectrum. The results from the long irradiation will be considered first, as they are the simplest and cleanest looking spectra. The additional peak in the short irradiation will then be analyzed and identified.

4.1.1 Long Irradiation Results

In all cases, the gamma spectra recorded after irradiation were very clean and appear to only indicate the presence of ^{65}Zn, which makes sense as the spectra were recorded approximately 10 days after the irradiation was finished and all of the other isotopes would have long since decayed. The spectra for sample M4 was recorded over 100 seconds and is shown in Fig. 15 to demonstrate the sharpness of the two visible peaks and the very low background level. The same spectrum is also shown on a semi-log scale in Fig. 16 to bring out additional features such as the Compton edge, Compton continuum and the backscatter peak, which are all visible, as predicted. The gamma spectra for the other samples are omitted because they are essentially identical, although the total number of counts will differ based on the fluence received as well as the length of the measurement.

At the time of measurement (10 days after irradiation) only two peaks are expected to be visible: the 511 keV peak from the annihilation of the positron emitted 1.42% of the time and the 1115.5 keV peak corresponding to the electron capture

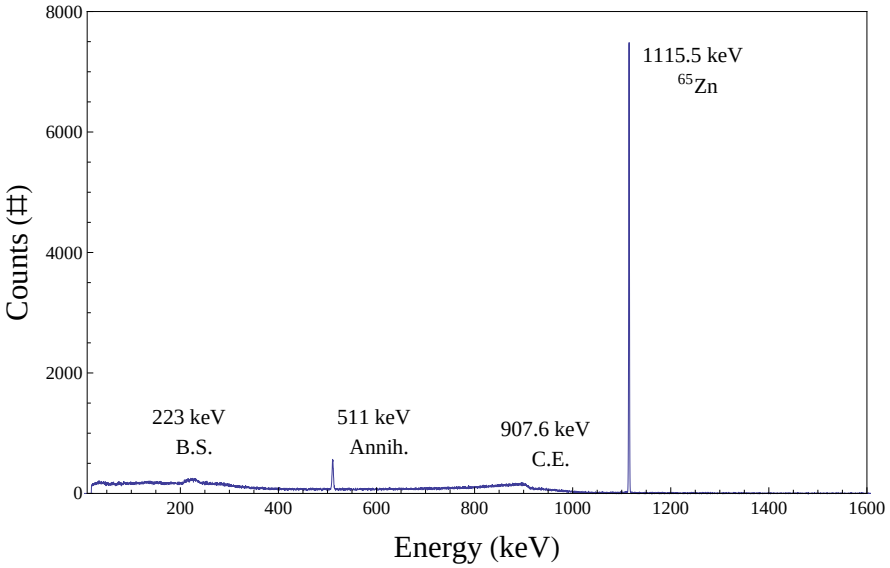

Figure 15. Linear Plot of Long Irradiation Gamma Spectrum

This plot of the gamma spectrum is on a linear scale to show the strength of the ^{65}Zn peak compared to the others.

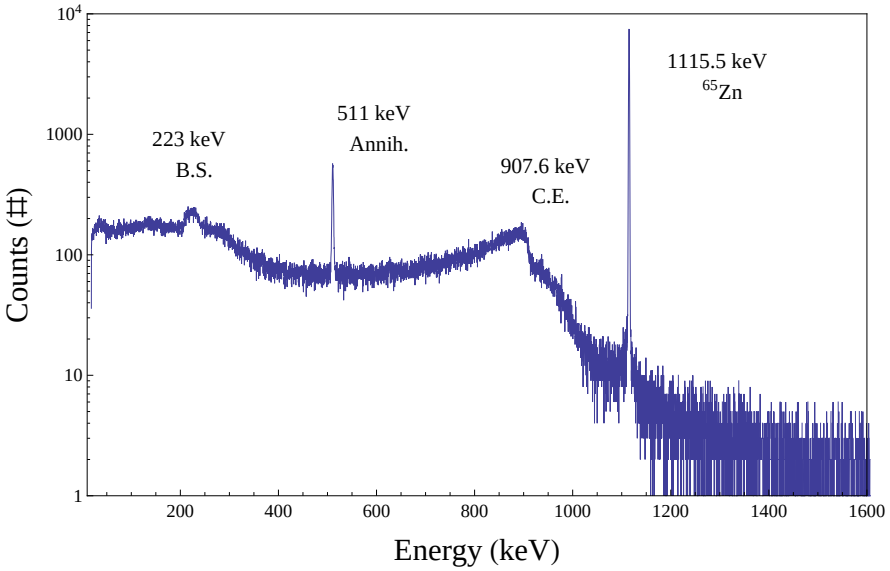

Figure 16. Semi-log Plot of Long Irradiation Gamma Spectrum

This is a plots of the gamma spectrum plotted on a semi-log scale to make more of the spectral features visible. On this scale the Compton edge and backscatter peak are clearly visible and are located in the proper position for ^{65}Zn.

decay of ^{65}Zn to the excited state of ^{65}Cu. Visually, the peaks in these spectra seem to coincide with the expected values but this needed to be verified.

4.1.1.1 Identification of 511 keV Annihilation Peak

First, the peak near 511 keV will be analyzed. This peak is singled out and shown in greater detail in Fig. 17, where a semi-log scale was chosen to highlight the background counts. The peak is definitely Gaussian, though not very smooth, with upper and lower bounds at 506 and 515 keV, respectively. The background in this region was found to be approximately 70 counts per channel, which was then subtracted from all of the channels being considered. Using Eq. 8, the centroid was found to be located at 510.728 keV which is close to, but not exactly 511 keV. There is one isotope that emits a γ-ray of this energy, ^{208}Ti (510.77 keV) [24], and many more that decay by β^+ that will result in a 511 keV annihilation peak. However, titanium can be ruled out because the short half life of the ^{208}Ti isotope (3.053 min) [24] means that it would have long since decayed away. In fact this must be an annihilation peak, which ^{65}Zn will produce, but it cannot be used alone to determine the presence of ^{65}Zn because many isotopes will decay by positron emission. The area of the peak was found to be 6592$\pm$81 counts, which will be compared to the other peak to determine whether the ratio of the two peaks agree with the known decay probabilities for ^{65}Zn.

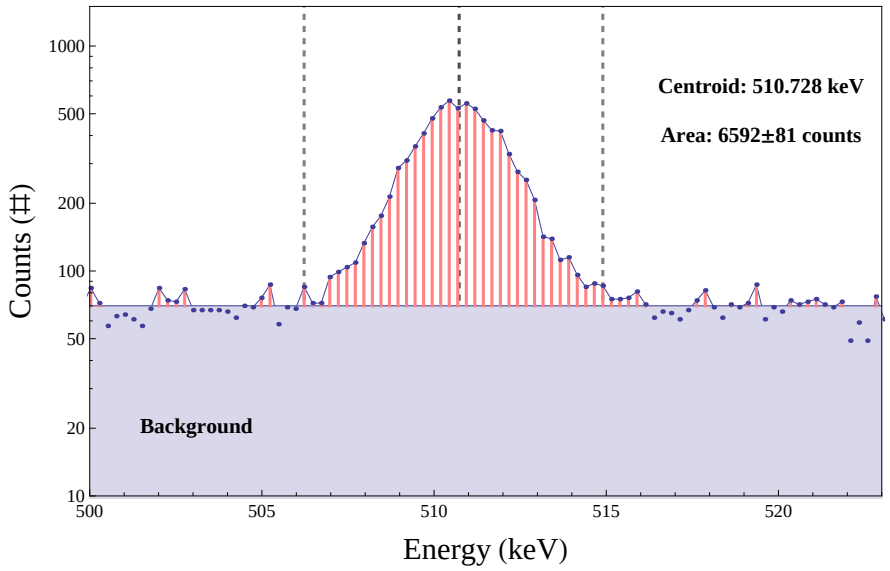

Figure 17. Peak Analysis of the 511 keV Region

This plot shows the analysis of the peak in the 511 keV region. The background count was highest in this region due to the Compton continuum, ∼70 counts per channel, and the centroid was found to be 510.73 keV, indicating the peak was due to positron annihilation. It is later shown that the proportion of this peak to the 1115 keV peak is in agreement with theory on the decay of ^{65}Zn. The total counts in the peak were found to be 6592±81, which, assuming this annihilation is only due to the low probability ^{65}Zn positron decay, gives an activity of 87.64±1.08 μCi.

4.1.1.2 Identification of 1115 keV ^{65}Zn Peak

The next peak to analyze is the large one, centered near 1115 keV. Again, this peak is singled out and shown in greater detail in Fig. 18. Now the peak is clearly Gaussian and very smooth which indicates plenty of counts were collected for good statistics. The background noise in this region is very small with a value of approximately 15 counts per channel. Once these counts are subtracted, the centroid is found, using Equation 8, to be 1114.98 keV. This is close to the expected value of 1115.5 keV but there are two other possibilities that need to be considered: ^{127}Sn (1114.3 keV) and ^{65}Ni (1115.5 keV) [24]. However, both ^{127}Sn and ^{65}Ni can be dismissed immediately because their short half-lives (2.1 hours and 2.5 hours, respectively [24]) mean they would have long since decayed away in these samples. The

slight offset from the expected energy value of 1115.5 keV is likely due to a slight deviation in the energy calibration of the detector. Finally, the area of the peak was found to be 54826±234 counts. This can be used with Equation 9 to determine that the activity of the ^{65}Zn isotope is 89.19±0.38 μCi.

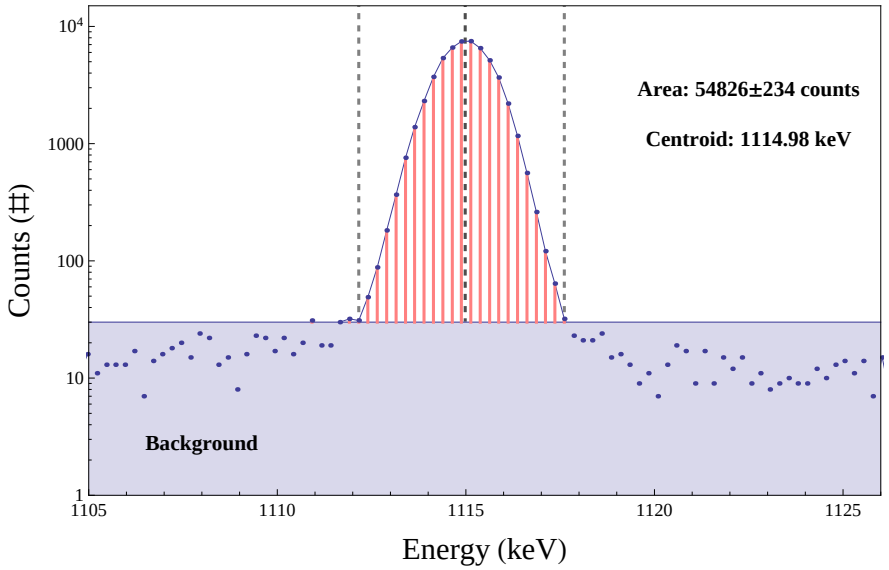

Figure 18. Peak Analysis of the 1115 keV Region
This plot shows the analysis of the peak in the 1115 keV region. The background count was very low in this region, ∼15 counts per channel, and the centroid was found to be 1114.98 keV, indicating the peak was due to the electron capture decay of ^{65}Zn. The total counts in the peak were found to be 54826±234, which gives an activity of 89.19±0.38 μCi.

To further verify that ^{65}Zn is the isotope being detected, the counts in the annihilation and 1115 keV peaks should be compared. If this is ^{65}Zn then 50.23% of the decays should result in a 1115 keV γ-ray and 1.42% should result in a positron which will create two 511 keV photons when it annihilates. Thus the ratio of the counts should be 2.82 to 50.23 or 0.0561. The total decays for each photon is

$$decays = \frac{C}{\epsilon_{abs}(h\nu)},$$

where C is the number of counts in the peak and $\epsilon_{abs}(h\nu)$ is the energy dependent absolute efficiency of the detector at the energy of the γ-ray being considered. This

gives the total number of each γ-ray emitted instead of only the fraction that was detected. This was 9.2×10^9 decays for the 1115 keV γ-ray and 1.6×10^8 decays for the 511 keV γ-ray. The ratio of these two numbers is 0.0559 which matches the expected value to the first three decimals. This signal is definitely due to ^{65}Zn decaying, which is known to decay only to ^{65}Cu.

4.1.1.3 Backscatter Peak and Compton Edge

The backscatter peak, shown in Fig. 19, is not a well formed peak, but is located between 206 and 240 keV which is the appropriate range [23]. The energy of the maximally Compton scattered 1115 keV γ-ray ($\theta = \pi$) can be found by Equation 7 to be 207.9 keV. This is the minimum energy of a Compton scattered photon from the 1115 keV γ-ray corresponding to a head-on collision with an electron and represents the low end of the backscatter peak. As collision angle decreases, less and less energy is lost in the Compton interaction and the resultant photons will be more energetic. Eventually, the angle of deflection will decrease enough that the Compton scattered photons are not directed back into the detector and this marks the upper bound of the peak, located at approximately 240 keV. Solving Equation 7 for the angle θ that will result in a 240 keV γ-ray finds the minimum deflection angle to be approximately $\frac{3}{4}\pi$.

The Compton edge is formed by the same process, except the scattering occurs in the material and the resultant photon is able to escape the material before its total energy is absorbed. This results in an energy measurement lower than the full energy peak by the energy of the photon lost. The minimum energy that can be lost was already calculated to be 207.9 keV for a 1115 keV photon and therefore the highest energy that can be measured when a Compton scattered photon escapes is 907.6 keV. This energy level marks the Compton edge and the measured data matches this predicted value precisely, as shown in Fig. 16. Unlike the backscatter peak, all

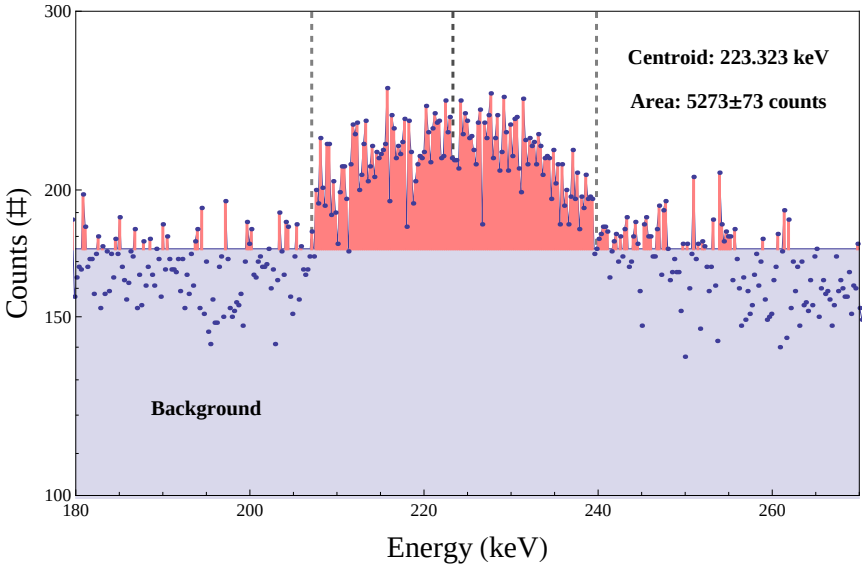

Figure 19. Peak Analysis of the Backscatter Region
This plot shows the analysis of the peak in the backscatter region. The background count was very high in this region due again to the Compton continuum, ∼175 counts per channel, and the centroid was found to be 223.3 keV, indicating the peak was due to the backscatter of a γ-ray interacting with the walls of the detector chamber and being scattered back into the detector.

angles of deflection can lead to the loss of a scattered photon, all the way down to a glancing collision which will result in a large loss for the detector. This leads to the higher background count region from 0 keV up to the Compton edge, known as the Compton continuum.

4.1.2 Short Irradiation Results

The short irradiation resulted in a similar gamma spectrum; as one would expect due to the similarity in the crystals. However, there is an additional peak in these spectra, as shown in Fig. 20, a plot of the gamma spectrum recorded over 600 seconds for sample S1 which was irradiated in the CIF for 5 hours. This sample was measured much sooner after irradiation (approximately 6 days), so a peak at 438 keV, corresponding to the ^{69m}Zn isomer is expected, but must be verified.

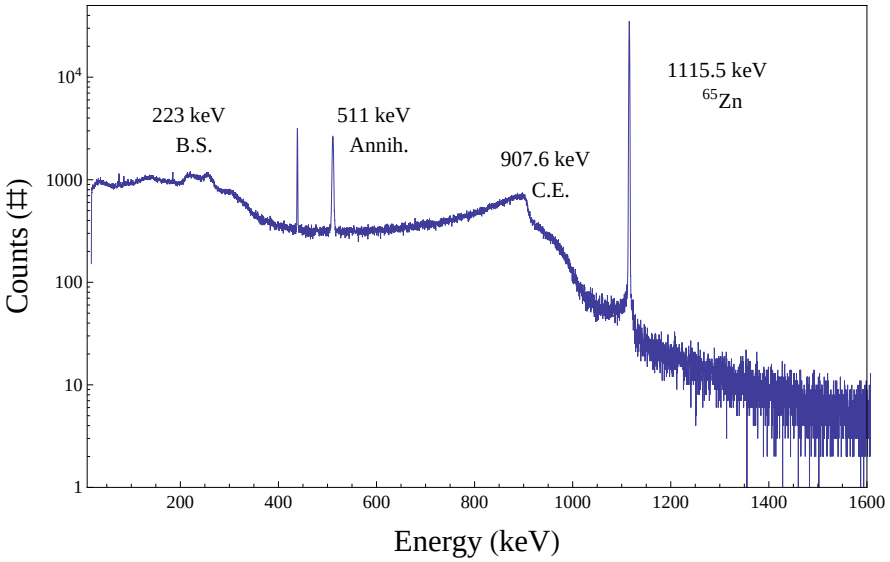

Figure 20. Semi-log Plot of Short Irradiation Gamma Spectrum

This plot resembles the spectrum for the long irradiation (Fig. 16) but has an additional peak at 438 keV corresponding to ^{69m}Zn. This isotope is seen because the short irradiation samples were measured much sooner than the long irradiation samples and the ^{69m}Zn isotope had not yet decayed away.

4.1.2.1 Identification of 438 keV ^{69m}Zn Peak

The only peak to analyze in the short irradiation sample is the peak near 438 keV as the other peaks and features were identified and discussed previously when analyzing the long irradiation samples. This peak is shown in greater detail in Fig. 21. As was done previously, the background was found to be approximately 350 counts per channel with upper and lower bounds of 437 keV and 442 keV respectively. This gave a peak centroid of 438.65 keV and an area of 15210±123 counts. The Table of Isotopes has three possibilities for this isotope: ^{237}Am (438.4 keV), ^{69m}Zn (438.6 keV) and ^{150}Eu (439.4 keV) [24]. The americium isotope can be ruled out due to its half-life (73 minutes [24]) as it would have already decayed away. Europium can also be dismissed because it has a very long half-life (39 years [24]) and it would still be visible in the long irradiation samples if it had created this peak. Therefore, this can only be due to the ^{69m}Zn isomer, as expected.

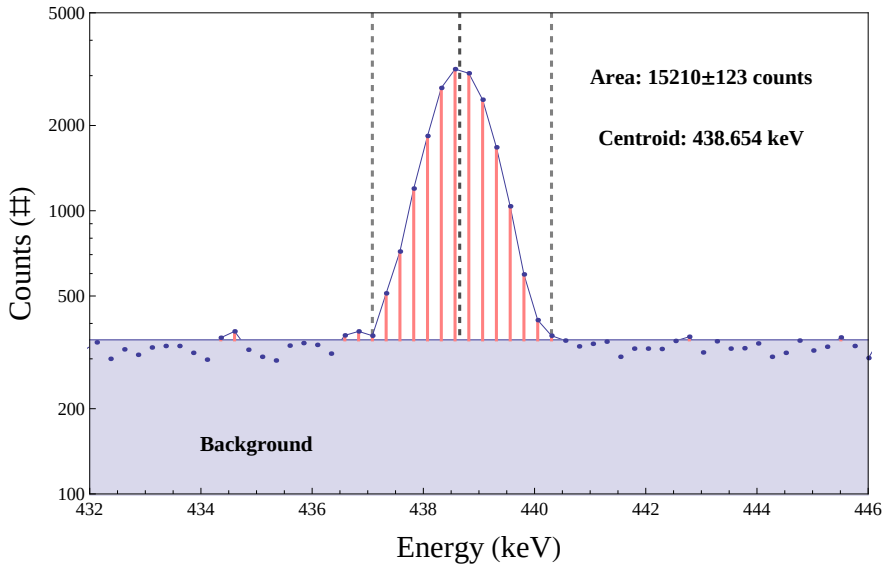

Figure 21. Peak Analysis of the 438 keV Region
This plot shows the analysis of the peak in the 438 keV region. The background count was very high in this region due to the Compton continuum and longer counting time, ∼350 counts per channel. The centroid was found to be 438.65 keV, indicating the peak was due to the internal transition of ^{69m}Zn to ^{69}Zn. The total counts in the peak were 15210±123, which gives an activitiy of 1.16±0.01 μCi.

4.1.3 Analysis of Sample Activities

The activities of the samples were calculated using Equation 9 and the counts in the ^{65}Zn and annihilation peaks. The two were then compared to further verify the activity. As can be seen in Table 6, the activity calculations from both peaks are within a few μCi showing fair agreement. The activity measured from the 1115 keV peak is likely to be more accurate for two reasons. The first is that it has more counts than the 511 keV peak which gives it a more Gaussian shape and better statistics. The second is that additional 511 keV γ-rays could be incident on the detector from decays other than the ^{65}Zn positron decay. Ultimately, the values from the 511 keV peak are just shown as rough estimates of activity that serve to support the activities calculated from the 1115 keV peaks.

Samples H1 and H3 were calculated differently, and did not have their spectra fully recorded. The three H samples (H1, H2 and H3) were all much larger than

Table 6. Predicted and Measured Activities After Irradiation

Sample	Time After Irradiation	Measured ^{65}Zn Activity from 1115 keV Peak [μCi]	Measured ^{65}Zn Activity from 511 keV Peak [μCi]	Measured ^{69m}Zn Activity from 438.6 keV Peak [μCi]
S1	6 days	89.46±0.18	92.68±0.54	1.16±0.01
S2	6 days	5.31±0.04	5.27±0.12	0.055±0.002
M3	11 days	66.61±0.33	65.29±0.93	-
M4	11 days	89.19±0.38	87.64±1.08	-
M5	11 days	1.38±0.01	1.26±0.04	-
M6	11 days	0.60±0.01	0.55±0.02	-
H1	11 days	162±1	-	-
H2	11 days	75.7±0.35	74.5±0.99	-
H3	11 days	265±1	-	-

the main Eagle Picher material and had much higher activations. H2's activity was low enough that it could be counted directly using all of the methods previously described. H1 and H3, however, had activities that were too high and resulted in large amounts detector dead time. To combat this a new geometry had to be chosen, one that had not been calibrated for and one that was not ideal.

The samples were placed outside of the detector cavity approximately a foot above the opening, with the lid open. This introduced enough distance that the detector no longer had massive amounts of dead time and was able to record an uncalibrated spectrum. Sample H2, which had already been found to have an activity of 75.7±0.35 μCi, was again recorded, this time in the new geometry, and the counts per second (cps) for the 1115 keV peak in this configuration was found to be 70.25. This gave a relationship for activity and cps in the new geometry: 1.078 μCi/cps. Samples H1 and H3 were then recorded in this geometry and found to have 150.62 cps and 245.46 cps, respectively. This gives an activity of 162±1 μCi for H1 and 265±1 μCi for H3.

These values can be checked by considering the specific activity for all the long irradiation samples in the CIF. Samples M3, M4, H1, H2 and H3 all received an

equivalent neutron fluence and should have had the same amount of activation per unit mass. Dividing all of the activities through by their masses gives a specific activity of 1.84±0.02. With such a small standard deviation the activities calculated in this new geometry agree well with those calculated more directly in the calibrated geometries.

4.1.3.1 Comparison of Measured Counts to Model Predictions

After identifying the peaks and determining the activity of the samples, a comparison can be made to the values predicted by the model described in Sec. 2.5. Samples H1 and H3 could not be compared because they were not measured in a calibrated state, but all of the remaining samples were considered. The counts predicted for each peak are compared to the counts recorded in Tables 7-9 and the total activity predicted is compared to the total activity measured in Table 10. The final column of all of these tables indicates the percent difference between the measured and predicted values with the sign indicating the direction of deviation from the measured number (i.e. "+" indicates the predicted number was higher and "-" indicates the predicted number was lower).

Table 7. Comparison of 438.6 keV Counts with Model

Sample	Measured	Predicted	Difference
S1	15210±123	14756±121	-3.0±1.1%
S2	738±27	1535±39	+108.0±6.5%
M3	0	0	0%
M4	0	0	0%
M5	0	0	0%
M6	0	0	0%
H2	0	0	0%

Table 8. Comparison of 511 keV Counts with Model

Sample	Measured	Predicted	Difference
S1	29660±172	28220±167	-4.9±0.8%
S2	1686±41	3637±60	+115.7±4.3%
M3	4911±70	5155±72	+5.0±2.0%
M4	6592±81	7007±84	+6.3±1.8%
M5	1236±35	3252±26	+163.1±5.4%
M6	1162±34	2934±54	+152.5±5.5%
H2	5600±75	5829±76	+4.1±1.9%

Table 9. Comparison of 1115.5 keV Counts with Model

Sample	Measured	Predicted	Difference
S1	255763±506	251055±498	-1.8±0.3%
S2	15172±123	32352±180	+113.2±1.4%
M3	41230±203	42242±206	+2.5±0.7%
M4	54826±234	57421±240	+4.7±0.6%
M5	10995±105	26129±162	+137.6±1.8%
M6	10161±101	23578±154	+132.0±1.8%
H2	46848±216	47772±218	+2.0±0.7%

Table 10. Comparison of Total Activity with Model

Sample	Measured	Predicted	Difference
S1	90.62±0.18	88.2 μCi	-2.7%
S2	5.36±0.04	11.5 μCi	+114.6%
M3	66.61±0.33	68.5 μCi	+2.8%
M4	89.19±0.38	93.2 μCi	+4.5%
M5	1.38±0.01	3.3 μCi	+139.1%
M6	0.60±0.01	1.4 μCi	+133.3%
H2	75.7±0.35	77.5 μCi	+2.4%

Ultimately, the model worked well in predicting the counts for each of the peaks and the total activity of the samples irradiated in the CIF, but grossly failed for the samples in the TC. The counts from the CIF samples were all within 6.3±1.8% of the predicted values, with the largest difference being from the 511 keV peak which did not develop into a well defined Gaussian distribution during the period of measurement. This confirms the assumptions made during the development of the

model were valid and resulted in reasonably reliable numbers. In fact, in almost all cases, the counts and activity predicted were higher than measured which gave an additional margin of safety when planning the irradiation.

The TC predictions, however, are very high, more than twice the values that were actually recorded. Only a few variables were changed between calculations for the two irradiation facilities and the flux is the only constant across the TC calculations that is different from the CIF calculations and the other variables (mass, time after irradiation, and time of measurement) do not appear to have had any impact on the variation between predicted and measured values. This seems to indicate that the flux provided for this region is incorrect, being reported too high by approximately a factor of two. A flux spectrum for the TC would have helped, but was not available.

In addition to counts and activity, the model made predictions on what the peaks of the spectra would look like. The predicted spectrum for sample S1 (5 hour CIF) is shown in Fig. 22 with the actual, measured spectrum overlaid as a series of red dots which correspond to the number counts recorded in a given channel.

This plot shows that the predicted spectrum closely matches the recorded spectrum and indicates that the model was able to predict which isotopes would still be visible and the relative heights of the resultant peaks. This model was not written to show features such as the backscatter peak, Compton edge or the Compton continuum; which are not visible in the predicted spectra. It was, however, written to determine how easy or difficult it would be to analyze the crystals after irradiation based on the constituent isotopes of ZnO and the known impurities. The model indicated that the analysis would be fairly simple with typically only 2-3 peaks depending on how quickly after irradiation the gamma spectrum was recorded and the measured spectra indicate these predictions were correct.

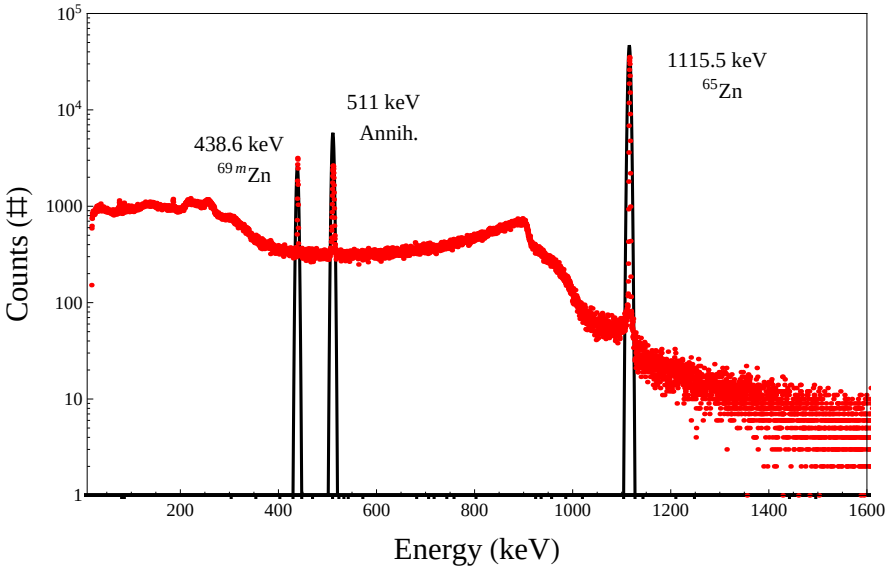

Figure 22. Comparison of Predicted Spectrum to Measured Spectrum
A comparison of the predicted spectrum (indicated by the three black Gaussian peaks) and the measured spectrum (indicated by red dots as discrete measurements). The height of the predicted peaks closely matches the height of the peaks recorded, despite the fact that the Gaussian peaks consider a continuous distribution of counts as opposed to a discrete distribution based on channel width.

4.1.4 Calculation of the ^{65}Cu Concentration

With the model giving predictions for the activities of the CIF samples that are within 17.3% of the measured values, this model can be used to develop a formula to predict the concentration of the ^{65}Cu in the sample in time. This is accomplished by integrating the activity calculated by the model over the time of interest starting with $t = 0$ at the start of irradiation. From the model, the concentration of ^{65}Cu is given as a piecewise solution,

$$C_{^{65}Cu}(t) = \begin{cases} \int_0^t C_{^{64}Zn}\,\sigma\,\Phi\,(1 - e^{\frac{-t'}{\tau}})\,dt' & t \le t_{irr} \\ \int_0^t C_{^{64}Zn}\,\sigma\,\Phi\,(1 - e^{\frac{-t_{irr}}{\tau}})\,(e^{\frac{t_{irr}-t'}{\tau}})\,dt' & t > t_{irr} \end{cases}, \qquad (12)$$

where C is the concentration of the isotope designated by the subscript, σ is the neutron absorption cross-section in barns for ^{64}Zn at 0.025 eV, Φ is the thermal neutron flux, t_{irr} is the time of irradiation and τ is the mean lifetime, or $\frac{t_{1/2}}{ln\,2}$, of

the unstable isotope ^{65}Zn. The first line will give concentrations of ^{65}Cu during irradiation, and the second line for times after the irradiation. A plot of this equation for the 20-hour, CIF irradiated samples is shown in Fig. 23.

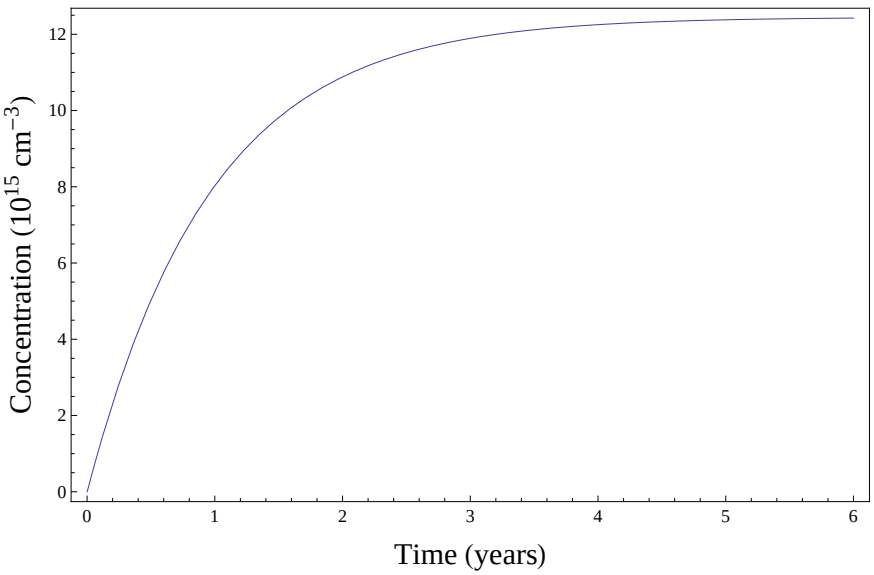

Figure 23. ^{65}Cu Concentration in CIF Samples in Time
The concentration of ^{65}Cu in the 20-hour neutron irradiated CIF samples is shown. The samples should stabilize roughly 3-4 years after the irradiation.

One of the difficulties in this experiment is the long half life of ^{65}Zn. The samples require several years for the copper concentration to begin to stabilize. Early on, the concentration is much smaller than it will ultimately achieve, but fortunately it was sufficient for EPR spectroscopy to detect the copper that was created as a result of the transmutation.

4.2 EPR Spectroscopy

EPR spectra were recorded for both the long and short irradiations, but there was little difference in the results. Unlike the gamma spectroscopy analysis, which needed to be recorded quickly after irradiation to measure the most signals, the samples being analyzed with EPR benefited by waiting as long as possible because this allowed more of the unstable ^{65}Zn to decay to ^{65}Cu and thus created a stronger

signal. Despite the fact that the short irradiation samples had an additional month to decay, the long irradiation samples had a stronger copper signal and will therefore be the focus of the EPR analysis.

The samples in the thermal column turned out to be rather uninteresting, as far as EPR is concerned, because they did not produce any EPR signal within the limited time available for this research. If the TC samples were allowed to cool for 1-3 half-lives then there might be some signals detected, but even the 20-hour TC samples had no signs of copper as shown in Fig. 24. As a result, the 20-hour CIF samples will be the only samples used in the analysis of the EPR spectra.

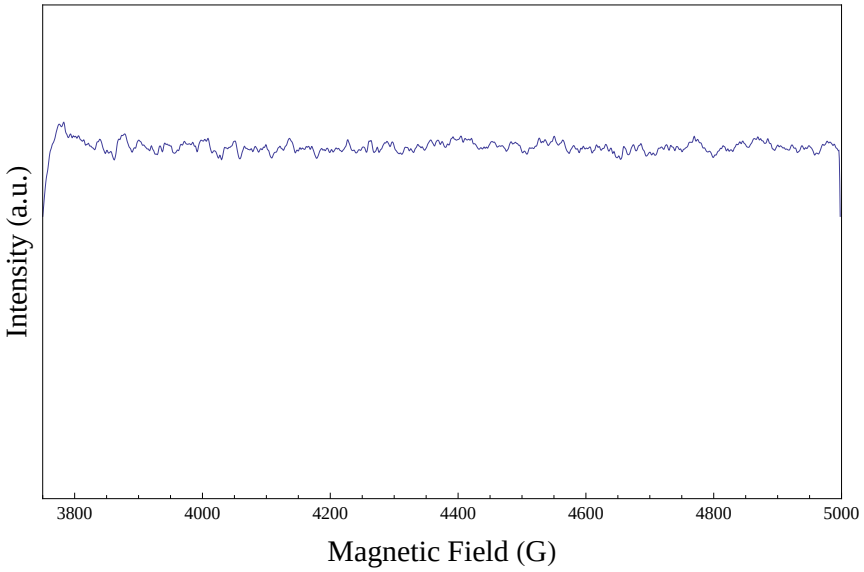

Figure 24. Post-irradiation EPR Spectrum for Sample M5
This EPR spectrum was recorded for sample M5. It was taken two months after the 20-hour irradiation in the TC and shows no detectable amount of copper present.

4.2.1 Spectrum Processing

The spectra shown in this section all received some slight processing to improve their appearance. The major problem was that at high magnetic field strength the baseline began to rise, as shown in Fig. 25. This was purely due to the spectrometer and did not indicate any abnormality in the sample or an additional signal. The

baseline was corrected by fitting a fourth-order polynomial to the spectra and then subtracting that from the recorded data. This straightened out the baseline and had no effect on the signals. The final adjustment performed was to use a three-point moving average to decrease the noise in the signal.

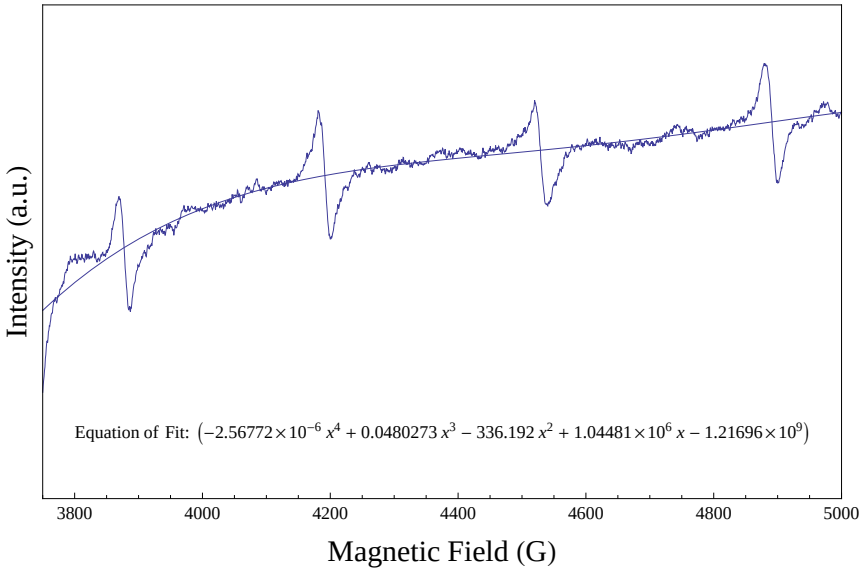

Figure 25. EPR Spectrum Without Baseline Adjusted
This plot demonstrates the rise in the baseline at high field strengths. This shift is corrected by fitting a fourth-order polynomial to the data and then subtracting that from the signal. The resultant spectrum can be seen in Fig. 28 and has a much more level baseline without any loss of signal information.

4.2.2 Spectra of Pre-Annealed Samples

Prior to irradiation, sample M3 was annealed to verify the presence of copper, which was detected by EPR with the assistance of a 442 nm laser. This was the only sample to be annealed prior to irradiation. The EPR spectrum recorded two months after the 20-hour irradiation is shown in Fig. 26 with no light incident on the sample. This spectrum shows four strong signals in the appropriate region with a spacing of 1013±1 G corresponding to the peak separation for the ^{65}Cu isotope as well as much smaller peaks with a spacing of 945±1 G. The peaks are not as well formed as those shown in Fig. 14, but they indicate the ^{65}Cu isotope quite clearly

and hint at the presence of ^{63}Cu.

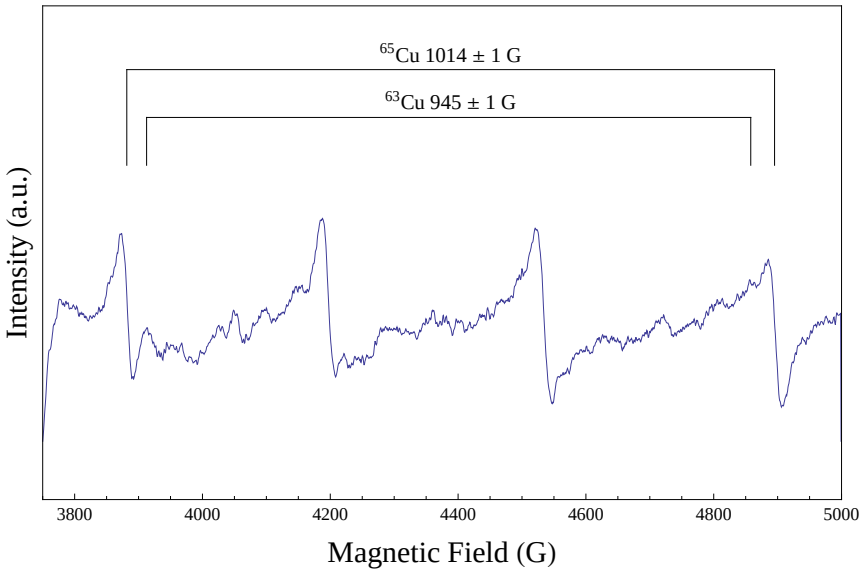

Figure 26. Post-irradiation EPR Spectrum for Sample M3 No Light
Even with no light to excite the native copper atoms, both isotopes are visible in this plot. This indicates that the Fermi level has been lowered and now some of the native copper can remain in the Cu^{2+} state without any laser light.

A second EPR spectrum (Fig. 27) was recorded for this sample with laser light (442 nm) to further reveal the copper that was present prior to irradiation. This spectrum shows a stronger peak at the low end and as well as a slightly stronger one on the high end. The separation for these two additional peaks is 946±1 G which corresponds to the ^{63}Cu isotope.

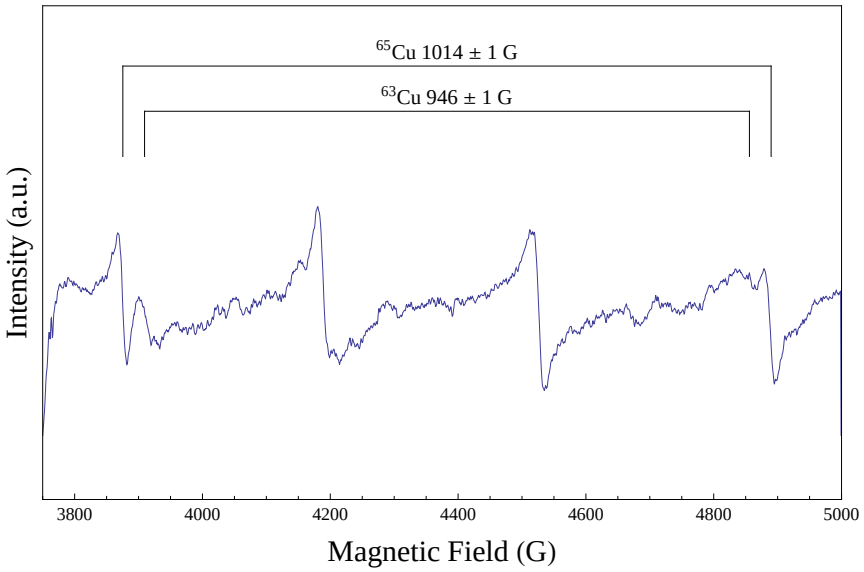

Figure 27. Post-irradiation EPR Spectrum for Sample M3
When laser light was supplied to the sample, more of the native copper atoms became visible.

Unlike the M2 reference sample, these CIF samples could not have their EPR spectra taken while being exposed directly to laser light because they had been discolored by the neutron irradiation and were thus heated above 9 K as they absorbed more of the energy from the laser beam. This heating was enough that the signal disappeared completely if the laser was aimed directly at the sample and still decreased the peak amplitude of the signals slightly when the laser light was positioned so that it scattered into the sample. Sample M2 was able to receive the beam directly and excite more of the initial copper because it was transparent and did not greatly heat. Since sample M3 did not receive the full energy of the laser, it is likely that not all of the initial copper atoms were excited to the Cu^{2+} state.

When this spectrum is combined with Fig. 26, which shows a strong ^{65}Cu signal and a smaller ^{63}Cu signal it is clear that the Fermi level has been lowered because now some of the native copper can be seen without laser light. The addition of laser light, however, does increase the ^{63}Cu to ^{65}Cu ratio. It is clear from these plots that much more ^{65}Cu has been created and therefore the isotopic ratio must have been

changed. The degree to which this ratio is changed cannot be precisely determined from this data set however.

4.2.3 Spectra of As-Grown Samples

The remaining samples were all as-grown material, which means they were not annealed at 900^{o} C in air before irradiation. These samples had very similar spectra, two of which are shown below in Fig. 28. The neutron-induced Cu^{2+} signals between samples agree well and the spacing between the outermost peaks is consistent with the value determined from the reference sample. Laser light did not make any of the native copper visible nor did it affect the signal besides a reduction in intensity due to heating, as described previously. The as-grown samples clearly show only one isotope has been produced by the neutrons and the result is a much cleaner looking spectrum than that of M3. There are several things these EPR spectra reveal about ZnO and the copper in it initially.

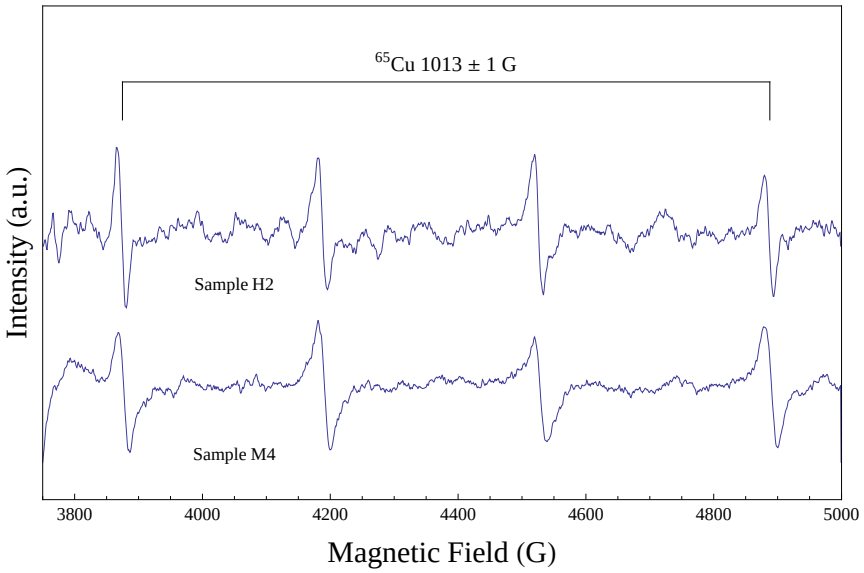

Figure 28. Post-irradiation EPR Spectra for Samples H2 and M4
In as-grown samples, the signal in the copper region is very clear and only shows one isotope (^{65}Cu). The separation of the outer peaks is measured to be 1013±1 G in agreement with the previously measured peak distance for ^{65}Cu.

The first is that copper must be above the Fermi level in this semiconducting material. As discussed in the theory section, the copper created in this transmutation is Cu^{2+} because of the orbital electron captured by the nucleus during the decay of ^{65}Zn. In other words, the $3d^{10}$ configuration of the transmuting ion becomes $3d^9$ when the orbital electron enters the nucleus. This $3d^9$ electron configuration has one unpaired electron ($S = 1/2$) that makes the atom paramagnetic and detectable via EPR spectroscopy. If copper were a shallow acceptor (below the Fermi level) then it would accept an electron and become a singly ionized Cu^{1+} acceptor. If this were the case, then an external stimulus (such as a laser) would be needed to excite the copper atoms to make them visible to EPR (i.e., the laser light would need to move an electron from the Cu^{1+} ion to a donor, where it would remain as long as the crystal is held at 25 K or lower). This is not happening, however, as the copper created via nuclear transmutation is always visible and therefore always in the Cu^{2+} state. This implies that copper exists above the Fermi level at 6 K and cannot donate any holes to the valence band.

These spectra also indicate that the copper native to the as-grown crystal as an impurity is not simply in the Cu^{1+} state, as was once thought [20]. If it were in this state then the data would suggest that the Fermi level has been lowered enough that Cu^{1+} should be able to shed an additional electron to become Cu^{2+}, which is clearly not the case or ^{63}Cu would be visible in these spectra. Clearly the annealing process required to view the native copper changes something about the configuration of the copper atoms within the crystal lattice. Only after this annealing is performed can the copper atoms be excited with a laser to become visible to EPR. The temperature of the reactor is not known, but it is apparently insufficient to cause this annealing process to occur during the irradiation, and thus the native copper remains unseen in the as-grown samples post-irradiation.

V. Conclusions

5.1 Summary of Results

After this research, there should be little doubt that the neutron irradiation of ZnO results in copper doping of the material. When ZnO is irradiated with neutrons, many interactions take place. The zinc, oxygen and impurity atoms will absorb neutrons probabilistically based on the energy of the neutrons and the cross-section for interaction. Theory tells us most of these interactions can be ignored because they either lead to stable products, are too short-lived to be detected by gamma spectroscopy (oxygen), or do not activate enough to be detectable (impurities). The zinc interaction, however, is important.

Zinc atoms can absorb a neutron and when they do their atomic mass will be increased by one, resulting in four unstable isotopes while the rest are stable. These unstable isotopes (^{65}Zn, ^{69}Zn, ^{69m}Zn and ^{71}Zn) will begin to decay. ^{71}Zn decays away very quickly and ^{69}Zn decays by β-emission, so neither of these were detected in this research. However, both ^{65}Zn and ^{69m}Zn were detected and positively identified using gamma spectroscopy, shown again in Fig. 29. These spectra clearly indicated the presence of ^{65}Zn at all times and ^{69m}Zn when the samples were measured within a few days of irradiation. The intensities of their peaks and their individual activities were compared to a model based on simple nuclear physics theory and found to be in close agreement differing by a maximum value of 6.3±1.8% for the samples irradiated in the CIF. Predictions for samples placed in the TC, however, were off by more than 100%, likely due to misreporting of the neutron flux in this region.

Prior to this effort it was known that copper exists in ZnO as an impurity [21], and it was shown by Garces *et al.* that this native copper could be made visible by annealing the sample in air at 900 °C and then exposing the sample to laser light while EPR spectra were recorded at low temperature (6-7 K) [20]. This result

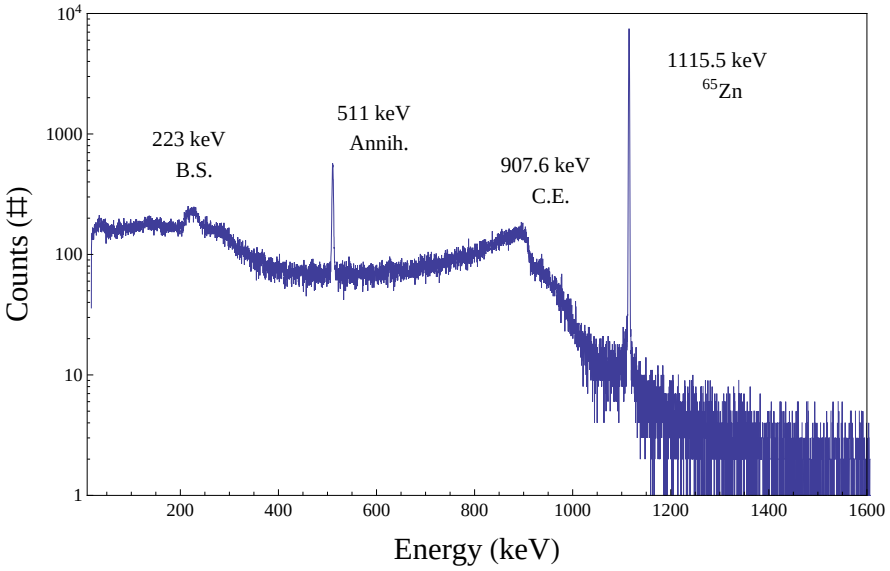

Figure 29. Semi-log Plot of Long Irradiation Gamma Spectrum

was replicated and the previously identified copper signal was used to determine the proper magnetic field region to search for new copper as well as to determine the spacing between signals for the two stable isotopes of copper. This spacing was found to be 1015±1 G for ^{65}Cu and 947±1 G for ^{63}Cu.

According to theory,^{65}Zn has three decay paths that all lead to ^{65}Cu [19]. This was confirmed by EPR spectroscopy as shown again in Fig. 30. In these samples, the native copper was not made visible because there was no anneal performed prior to irradiation and the CIF did not approach temperatures high enough to make the native copper visible. With and without laser light, the EPR spectra were the same for the as-grown crystals post-irradiation. Using the results found for the separation of the isotope signals it was simple to confirm the presence of only ^{65}Cu in these samples after irradiation.

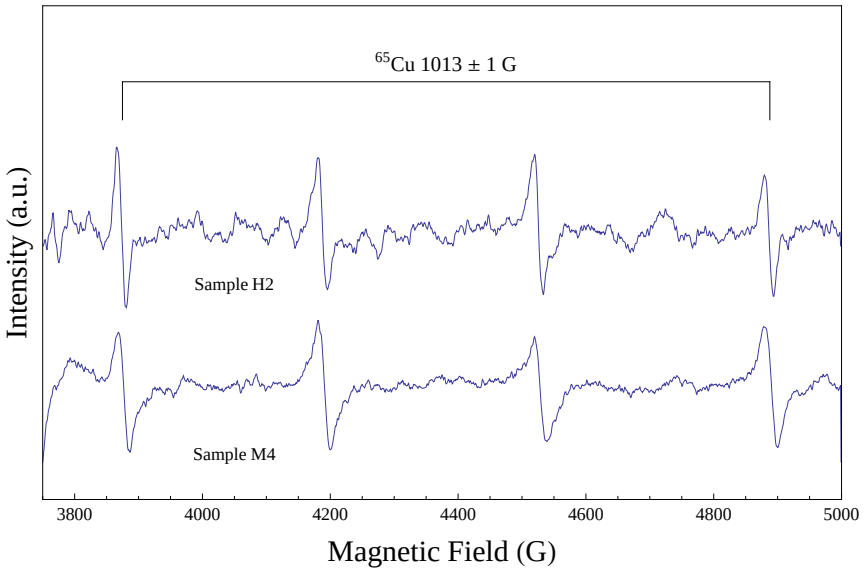

Figure 30. Post-irradiation EPR Spectra for Samples H2 and M4

The fact that the transmuted copper is visible at 6 K with no additional excitation implies that it is above the Fermi level and remains in the Cu^{2+} state in which it was created. Additionally, sample M3, which was annealed prior to irradiation showed some ^{63}Cu after irradiation without any laser light excitation, though the laser light did strengthen the ^{63}Cu peak. This means that some of the native copper was able to stay in the Cu^{2+} state, providing more evidence that the Fermi level was lowered as a result of the neutron irradiation. This further implies that the copper created exists above the Fermi level and may not provide holes to the valence band and might not increase the p-like nature of the material. Despite these implications, there is not yet enough information to determine the precise location of the copper atoms within the zinc oxide band gap and further study is needed to determine the true effect of copper doping on the conductivity of zinc oxide.

However, as was discussed in Sec. 1.3, if the copper doped into ZnO remains in the Cu^{2+} state it may have interesting possibilities as a DMS. While the ferromagnetic nature of Cu-doped ZnO is anything but certain [7–10], there may be a use for doping ZnO with copper via NTD.

5.2 Future Work

5.2.1 Verifying the Fermi Level

Before completely ruling out copper doping of ZnO as a potential path to p-type material, the position of copper within the band gap should be thoroughly studied. The fact that not all of the native copper in sample M3 is in the Cu^{2+}state may imply that after irradiation the the Fermi level is lowered to be close to the position of copper. If this is the case, annealing the sample to remove defects may result in a raising of the Fermi level and may change how the copper behaves. Hall measurements should also be taken to determine the carrier concentrations and whether the Cu-doping had any effect on the carriers.

5.2.2 Verifying the Ferromagnetic Behavior of Cu-doped ZnO

It has been suggested that copper doped in zinc oxide might have ferromagnetic behavior at room temperature. There is no consensus yet on this behavior and a thorough study of ZnO doped with copper as well as other transition metals would be of interest. Copper is of special interest though, because the ferromagnetic behavior is believed to occur when a doubly ionized copper atom replaces a zinc atom in the crystal lattice [9]. Doping via nuclear transmutation provides these two conditions exactly.

5.2.3 Understanding the Native Copper

What causes the native copper to be visible and invisible in ZnO is not well understood and this should be examined. It is known that heating at 900 °C is sufficient to make the copper atoms visible, but not without the additional excitation from a laser. The exact temperature where copper becomes visible with laser light is not known but could be found by a systematic annealing at various temperatures. If

the anneal is indeed driving apart a complex defect then IR absorption or some other experimental technique used in conjunction with EPR at each temperature step may be able to determine what that defect is. Additionally, the minimum energy to excite the copper atoms from $Cu^{1+}$to Cu^{2+} after the anneal should be determined by using light sources of various wavelengths. This might help determine the position of the singly ionized copper atoms in the band gap.

5.2.4 Irradiation of Other Semiconductor Materials

One final area of future work would be to examine NTD of other semiconductor materials. This should focus on creating n- or p-type materials, but might also look for materials that might display ferromagnetic behavior for a DMS. Almost any semiconductor would be of interest and a large study that looks at many semiconductor materials briefly might be able to identify a few materials that would be worthy of more in-depth investigation.

Bibliography

[1] D. C. Look, *Materials Science and Engineering: B*, vol. 80, p. 383, 2001.

[2] F. A. Selim, M. C. Tarun, D. E. Wall, L. A. Boatner, and M. D. McCluskey, *Applied Physics Letters*, vol. 99, 2011.

[3] I. S. Shlimak, *Physics of the Solid State*, vol. 41, pp. 716–719, 1999.

[4] W. E. Haas and M. S. Schnoller, *Journal of Electronic Materials*, vol. 5, p. 57, 1975.

[5] H. Kim, K. Park, B. Min, J. Soo Lee, K. Cho, S. Kim, H. Soo Han, S. Ku Hong, and T. Yao, *Nuclear Instruments and Methods in Physics Research B*, vol. 217, p. 429, 2004.

[6] J. G. Reynolds, C. L. Reynolds Jr, A. Mohanta, J. F. Muth, J. E. Rowe, H. O. Everitt, and D. E. Aspnes, "Shallow acceptor complexes in p-type zno," *Applied Physics Letters*, vol. 102, no. 15, p. 152114, 2013. [Online]. Available: http://scitation.aip.org/content/aip/journal/apl/102/15/10.1063/1.4802753

[7] A. Tiwari, M. Snure, D. Kumar, and J. T. Abiade, "Ferromagnetism in cu-doped zno films: Role of charge carriers," *Applied Physics Letters*, vol. 92, no. 6, p. 062509, 2008.

[8] D. B. Buchholz, R. P. H. Chang, J. Song, and J. Ketterson, "Room-temperature ferromagnetism in cu-doped zno thin films," *Applied Physics Letters*, vol. 87, no. 8, p. 082504, 2005.

[9] D. Chakraborti, J. Narayan, and J. Prater, "Room temperature ferromagnetism in zn1-xcuxo thin films," *Applied Physics Letters*, vol. 90, no. 6, pp. 062 504–062 504–3, 2007.

[10] Z. Jin, T. Fukumura, M. Kawasaki, K. Ando, H. Saito, T. Sekiguchi, Y. Z. Yoo, M. Murakami, Y. Matsumoto, T. Hasegawa, and H. Koinuma, "High throughput fabrication of transition-metal-doped epitaxial zno thin films: A series of oxide-diluted magnetic semiconductors and their properties," *Applied Physics Letters*, vol. 78, no. 24, pp. 3824–3826, 2001.

[11] J. L. G. Fierro, Ed., *Metal Oxides: Chemistry and Applications*. Boca Raton, FL: CRC Press, 2006.

[12] F. A. Selim, M. H. Weber, D. Solodovnikov, and K. G. Lynn, *Physical Review Letters*, vol. 99, p. 085502, 2007.

[13] C. G. Van de Walle, *Physical Review Letters*, vol. 85, p. 1012, 2000.

[14] F. Tuomisto, V. Ranki, K. Saarinen, and D. C. Look, *Physical Review Letters*, vol. 91, p. 205502, 2003.

[15] M. Herman. (2013) Brookhaven national lab: National nuclear data center. [Online]. Available: http://www.nndc.bnl.gov/sigma/

[16] K. S. Krane, *Introductory Nuclear Physics*. Hoboken, NJ: John Wiley and Sons, 1988.

[17] A. Sonzogni. (2013) Brookhaven national lab: National nuclear data center. [Online]. Available: http://www.nndc.bnl.gov/chart/

[18] S. S. Zumdahl and S. A. Zumdahl, *Introductory Nuclear Physics*, 5th ed. Boston, MA: Houghton Mifflin Company, 2000.

[19] M. M. Be, V. Christe, C. Dulieu, E. Browne, C. Baglin, V. Chechev, N. Kuzmenco, R. Helmer, F. Kondev, D. MacMahon, and K. B. Lee, *Table of Radionuclides*, vol. 3, 2006.

[20] N. Y. Garces, L. Wang, L. Bai, N. C. Giles, L. E. Halliburton, and G. Cantwell, *Applied Physics Letters*, vol. 81, pp. 622–624, 2002.

[21] R. E. Dietz, H. Kamimura, M. D. Sturge, and A. Yariv, "Electronic structure of copper impurities in zno," *Phys. Rev.*, vol. 132, pp. 1559–1569, Nov 1963. [Online]. Available: http://link.aps.org/doi/10.1103/PhysRev.132.1559

[22] M. M. Be, V. Christe, C. Dulieu, X. Mougeot, V. Chechev, N. Kuzmenco, F. G. Kondev, A. Luca, M. Galan, A. L. Nichols, A. Arinc, A. Pearce, X. Huang, and B. Wang, *Table of Radionuclides*, vol. 6, 2011.

[23] G. F. Knoll, *Radiation Detection and Measurement*, 4th ed. Hoboken, NJ: John Wiley and Sons, 2010.

[24] R. B. Firestone, *Table of Isotopes. 8th Edition: 1999 Update*, C. M. Baglin and S. Y. F. Chu, Eds. Hoboken, NJ: John Wiley and Sons, 1999.

[25] M. McCluskey and S. Jokela, "Sources of n-type conductivity in zno," *Physica B: Condensed Matter*, vol. 401, pp. 355–357, 2007.

[26] OSU. (2013) Ohio state university research reactor. [Online]. Available: http://reactor.osu.edu/facilities/research-reactor

[27] R. Eisberg and R. Resnick, *Quantum Physics of Atoms, Molecules, Solids, Nuclei, and Particles*, 2nd ed. Hoboken, NJ: John Wiley and Sons, 1985.

[28] J. P. McKelvey, *Solid State Physics for Engineering and Materials Science*, revised ed. Malabar, FL: Krieger Publishing Company, 2003.

[29] R. T. Weber, J. J. Jiang, and D. P. Barr, *EMX User's Manual*, 2nd ed., Bruker Instruments, Inc: EPR Division, Billerica, MA, 1998.

[30] D. A. Buchanan, *EPR and ENDOR Studies of Point Defects in Lithium Tetraborate Crystals*, Air Force Institute of Technology, Wright-Patterson AFB, OH3, 2012.

[31] M. A. Omar, *Elementary Solid State Physics: Principles and Applications*, revised ed. Reading, MA: Addison-Wesley Publishing Company, 1993.

REPORT DOCUMENTATION PAGE

Form Approved
OMB No. 0704-0188

PLEASE DO NOT RETURN YOUR FORM TO THE ABOVE ADDRESS.

1. REPORT DATE *(DD-MM-YYYY)*	2. REPORT TYPE	3. DATES COVERED *(From - To)*
27-03-2014	Master's Thesis	MAY 2012 - MAR 2014

4. TITLE AND SUBTITLE

Copper Doping of Zinc Oxide by Nuclear Transmutation

5a. CONTRACT NUMBER

5b. GRANT NUMBER

5c. PROGRAM ELEMENT NUMBER

6. AUTHOR(S)

Recker, Matthew C., Capt, USAF

5d. PROJECT NUMBER

14P168

5e. TASK NUMBER

5f. WORK UNIT NUMBER

7. PERFORMING ORGANIZATION NAME(S) AND ADDRESS(ES)

Air Force Institute of Technology
Graduate School of Engineering and Management (AFIT/EN)
2950 Hobson Way
Wright-Patterson AFB OH 45433-7765

8. PERFORMING ORGANIZATION REPORT NUMBER

AFIT-ENP-14-M-30

9. SPONSORING/MONITORING AGENCY NAME(S) AND ADDRESS(ES)

POC: MAJ Thomas McQuary (thomas.mcquary@dtra.mil)

Defense Threat Reduction Agency
8725 John J. Kingman Rd
Ft. Belvoir, VA 22060

10. SPONSOR/MONITOR'S ACRONYM(S)

DTRA

11. SPONSOR/MONITOR'S REPORT NUMBER(S)

12. DISTRIBUTION/AVAILABILITY STATEMENT

DISTRIBUTION STATEMENT A. Approved for public release; distribution is unlimited.

13. SUPPLEMENTARY NOTES

This material is declared a work of the U.S. Government and is not subject to copyright protection in the United States.

14. ABSTRACT

This research verifies that neutron irradiation of zinc oxide leads to Cu-doping of the material by nuclear transmutation. After irradiation, both Zn-65 and Zn-69m were detected and positively identified. Zn-65 was visible at all times while Zn-69m was visible when the samples were measured within a few Zn-69m half-lifes. All decay paths of Zn-65 lead to Cu-65 and the detection of the 1115.5 keV characteristic gamma ray from this decay clearly indicated that Cu-65 was being created. Previous electron paramagnetic resonance (EPR) spectroscopic results were replicated to determine the spectrum of copper impurities in ZnO as well as the corresponding spacing between signals in the hyperfine spectrum for the two stable isotopes of copper. This spacing was found to be 1015±1 G for Cu-65 and 947±1 G for Cu-63. The separation of EPR signals in the Cu hyperfine spectrum measured after neutron irradiation of the samples was found to be 1013±1 G confirming the creation of only Cu-65 during irradiation, as predicted by theory

15. SUBJECT TERMS

nuclear transmutation, doping, NTD, zinc, oxide, EPR, gamma spectroscopy

16. SECURITY CLASSIFICATION OF:			17. LIMITATION OF ABSTRACT	18. NUMBER OF PAGES	19a. NAME OF RESPONSIBLE PERSON
a. REPORT	b. ABSTRACT	c. THIS PAGE			Dr. John McClory AFIT/ENP
U	U	U	UU	84	19b. TELEPHONE NUMBER *(Include area code)* (937) 255-3636 x 7308 john.mcclory@us.af.mil